

Contents lists available at ScienceDirect

Comput. Methods Appl. Mech. Engrg.

journal homepage: www.elsevier.com/locate/cma





A modular framework for implicit 3D–0D coupling in cardiac mechanics

Aaron L. Brown ^{a,c}, Matteo Salvador ^{b,c,d}, Lei Shi ^{g,h}, Martin R. Pfaller ^{b,c,d}, Zinan Hu ^a, Kaitlin E. Harold ^f, Tzung Hsiai ⁱ, Vijay Vedula ^{g,*}, Alison L. Marsden ^{a,b,c,d,e,**}

- ^a Department of Mechanical Engineering, Stanford University, Stanford, CA, USA
- ^b Institute for Computational and Mathematical Engineering, Stanford University, Stanford, CA, USA
- ^c Stanford Cardiovascular Institute, Stanford, CA, USA
- ^d Department of Pediatrics (Cardiology), Stanford University, Stanford, CA, USA
- e Department of Bioengineering, Stanford University, Stanford, CA, USA
- f Department of Computer Science, Stanford University, Stanford, CA, USA
- g Department of Mechanical Engineering, Columbia University, New York, NY, USA
- ^h Department of Mechanical Engineering, Kennesaw State University, Marietta, GA, USA
- ¹ Department of Bioengineering, University of California Los Angeles, Los Angeles, CA, USA

ARTICLE INFO

Keywords: Cardiovascular modeling Cardiac mechanics 3D–0D coupling Multi-domain modeling Approximate Newton Method

ABSTRACT

In numerical simulations of cardiac mechanics, coupling the heart to a model of the circulatory system is essential for capturing physiological cardiac behavior. A popular and efficient technique is to use an electrical circuit analogy, known as a lumped parameter network or zerodimensional (0D) fluid model, to represent blood flow throughout the cardiovascular system. Due to the strong physical interaction between the heart and the blood circulation, developing accurate and efficient numerical coupling methods remains an active area of research. In this work, we present a modular framework for implicitly coupling three-dimensional (3D) finite element simulations of cardiac mechanics to 0D models of blood circulation. The framework is modular in that the circulation model can be modified independently of the 3D finite element solver, and vice versa. The numerical scheme builds upon a previous work that combines 3D blood flow models with 0D circulation models (3D fluid-0D fluid). Here, we extend it to couple 3D cardiac tissue mechanics models with 0D circulation models (3D structure-0D fluid), showing that both mathematical problems can be solved within a unified coupling scheme. The effectiveness, temporal convergence, and computational cost of the algorithm are assessed through multiple examples relevant to the cardiovascular modeling community. Importantly, in an idealized left ventricle example, we show that the coupled model yields physiological pressure-volume loops and naturally recapitulates the isovolumic contraction and relaxation phases of the cardiac cycle without any additional numerical techniques. Furthermore, we provide a new derivation of the scheme inspired by the Approximate Newton Method of Chan (1985), explaining how the proposed numerical scheme combines the stability of monolithic approaches with the modularity and flexibility of partitioned approaches.

^{*} Corresponding author at: Department of Mechanical Engineering, Columbia University, New York, NY, USA.

^{**} Corresponding author at: Department of Pediatrics (Cardiology), Stanford University, Stanford, CA, USA. E-mail addresses: vv2316@columbia.edu (V. Vedula), amarsden@stanford.edu (A.L. Marsden).

1. Introduction

Numerical simulations have long been used to investigate the cardiovascular system in both health and disease [1]. These efforts have primarily applied computational fluid dynamics (CFD) to study blood flow in the heart and vasculature [2–7], computational solid dynamics (CSD) to simulate tissue mechanics in the heart and vasculature [8–12], and fluid–structure interaction (FSI) for coupled problems [13–16]. Because accounting for the entire 3D circulatory system is typically infeasible due to limited imaging domains and a vast range of scales (micro- to macro-vessels), it is common to model parts of this system with a lumped parameter network (LPN), which can be thought of as a 0D model of blood flow. This treats blood flow in the circulatory system analogously to the flow of current in an electrical circuit [17] and allows one to quantify bulk quantities — pressure and flowrate — at various locations in the system, at a fraction of the cost of fully-resolved 3D CFD simulations. Representing some parts of the cardiovascular system — for example, the heart or specific blood vessels — with 3D structural and/or fluid models, while modeling the remainder using a 0D LPN constitutes a multi-domain approach [18,19]. The 0D LPN acts as a boundary condition on the 3D model that recapitulates physiological effects not captured by other, simpler conditions (e.g., zero-pressure). Coupling 3D and 0D models is the focus of this work.

Existing 3D–0D coupling approaches can be broadly categorized as monolithic [18,20,21] or partitioned [22–25]. Monolithic schemes are robust and generally exhibit better convergence properties, but are not conducive to modularity. We define modular schemes as those in which the 3D and 0D equations are solved separately by independent codes optimized for their respective problems, and those codes exchange information as needed to couple the two sets of equations. Partitioned approaches are typically modular, but may suffer from numerical stability issues. Past approaches can also be categorized by whether the 3D model is a fluid or a structure. Many studies have coupled 3D blood flow in large vessels to 0D circulation models [17–19], while many others have coupled 3D finite element models of the heart to 0D circulation models [11,24,26,27]. While these two problems, 3D fluid–0D fluid and 3D structure–0D fluid, are related, to the best of our knowledge, none have previously treated them in a unified manner.

Partitioned 3D structure–0D fluid schemes suffer from a particular issue known in the FSI literature as the balloon or incompressibility dilemma [22,28]. This issue arises in situations where the fluid is entirely enclosed by Dirichlet boundary conditions and the structure. In cardiac mechanics simulations, this manifests during the two isovolumic phases of the cardiac cycle, when both the inlet and outlet valves of the left ventricle (LV) are closed. The LV volume is nearly constant, but the LV pressure increases or decreases greatly due the contraction or relaxation of the heart muscle. In this situation, partitioned schemes that alternate between structure and fluid solvers typically fail because the structure solver is not aware of the constant-volume constraint. The balloon dilemma can be avoided by adopting a monolithic Newton approach, as in [20], in which a 3D model of the left and right ventricles was coupled to a closed-loop LPN. However, owing to their ease of implementation, partitioned approaches, with appropriate modification, have also been used. Early work in [25] avoided the balloon dilemma using a special iterative process that involved estimating the compliance of their 3D biventricular model. In [22], the authors addressed the issue by using a time-staggered approach, at each timestep determining the deformation of their LV model under a cavity volume constraint obtained from the 0D fluid. A similar approach was taken in [24]. Under certain conditions, this scheme leads to unphysical oscillations in time, which can be mitigated by the addition of a stabilization term [29]. The stabilized scheme was recently used to couple an electromechanical whole heart model to a closed-loop LPN [11].

In [19], the authors developed a hybrid approach to the 3D fluid–0D fluid coupling problem, combining the advantages of monolithic and partitioned approaches. This method was implemented in the open source multiphysics finite element solver svFSI (https://github.com/SimVascular/svFSI) [30] and has been used extensively in blood flow simulations where the solution in the 3D domain is strongly influenced by the surrounding vascular system [31–33].

In this work, we describe a modular numerical scheme to implicitly couple 3D fluid and/or structural mechanics models to 0D LPNs of the cardiovascular system. The algorithm was originally described in [19] for only the 3D fluid–0D fluid problem. Here, we extend it to solve the 3D structure–0D fluid problem, showing that these two problems can be treated under a unified coupling framework. The algorithm involves iteratively passing interface pressures and flowrates between the 3D and 0D solvers until both are converged in a given timestep. We additionally compute the interface resistance, defined as the change in pressure for a given change in flowrate, seen by the 3D model due to the 0D fluid. The tangent matrix in the 3D solver is modified according to this resistance, greatly improving convergence behavior and avoiding the balloon dilemma. Applying this coupling to an idealized left ventricle model, we demonstrate the method produces a realistic pressure–volume loop and naturally captures the isovolumic cardiac phases and opening and closing of valves without additional numerical treatment. We further derive the coupling scheme as a modification to the monolithic Newton approach, inspired by the Approximate Newton Method (ANM) of Chan [34], revealing a firm mathematical foundation. This connection to ANM also makes clear how the present coupling retains the robustness of a monolithic approach within a modular implementation like a partitioned approach. The modularity greatly improves usability, allowing the user to modify the 0D LPN independently of the 3D solver and vice versa.

The paper is organized as follows. In Section 2, the proposed coupling framework is derived. In Section 3, we leverage our numerical scheme in three different test cases, including an ellipsoidal LV coupled to an open-loop LPN, a spherical shell inflated through a limit point, and a pulmonary arterial model coupled to a closed-loop LPN. We also provide preliminary results on the convergence and computational cost of our method. In Section 4, we consider our method in relation to recent works and discuss limitations and future directions. Finally, in Section 5, we summarize our findings with respect to the proposed scheme.

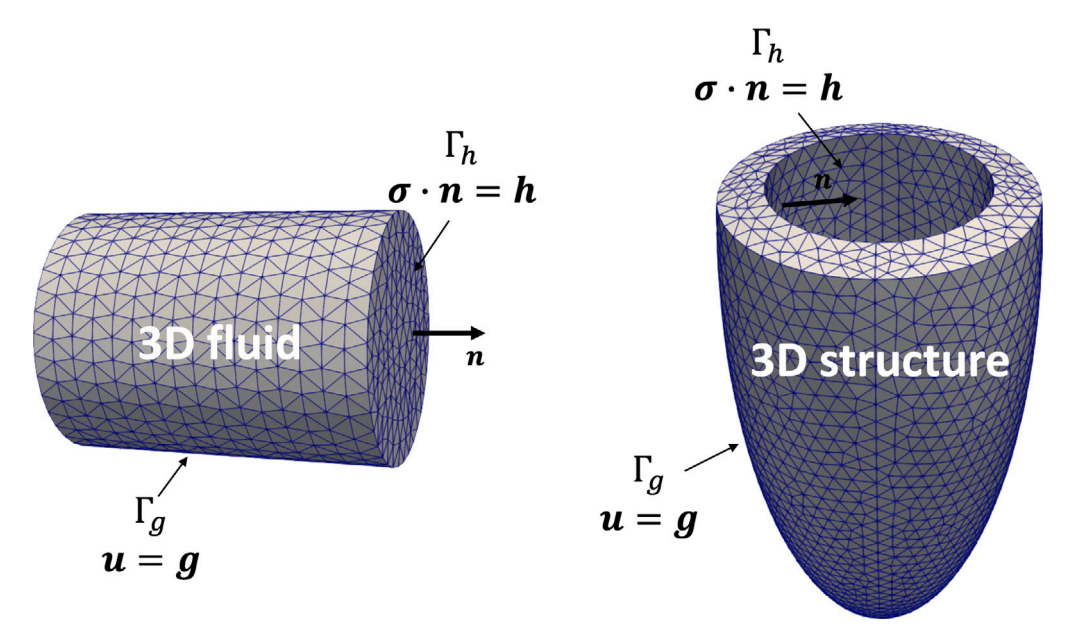


Fig. 1. Left: An idealized geometry of a section of a blood vessel is given as an example 3D fluid domain. Right: An idealized geometry of the LV of the heart is given as an example 3D structure domain. The dynamics in each are described by standard governing partial differential equations (PDEs), and on both, we may define Dirichlet or Neumann boundary conditions, or a combination of both. In this work, the PDEs are spatially discretized using the finite element method.

2. Methods

In this section, we derive the proposed coupling framework. The resulting equations are the same as those given in [19,35], but a generalized mathematical derivation, inspired by ANM [34] and applicable to both 3D fluid and 3D structure problems, is provided here. First, we state the governing equations for the 3D and 0D systems, then we describe how the two systems are mathematically coupled, and finally, we explain how to solve the coupled problem in a modular manner. In the following, the minor differences in the equations when considering a 3D fluid versus a 3D structure are highlighted.

2.1. 3D mechanical model: fluid or structure

We first state the governing equations and numerical formulation for an incompressible and Newtonian fluid on a fixed 3D domain [19], which models blood flow in large blood vessels (Fig. 1 left). Specifically, the Navier–Stokes equations, consisting of the momentum and continuity equations, as well as the Newtonian constitutive model, read

$$\rho \frac{\partial \mathbf{u}}{\partial t} + \rho \mathbf{u} \cdot \nabla \mathbf{u} - \nabla \cdot \boldsymbol{\sigma} - \mathbf{f} = \mathbf{0},\tag{1}$$

$$\nabla \cdot \mathbf{u} = 0, \tag{2}$$

$$\sigma = -p\mathbf{I} + \mu(\nabla \mathbf{u} + \nabla \mathbf{u}^T),\tag{3}$$

with boundary conditions

$$\mathbf{u} = \mathbf{g}, \ \mathbf{x} \in \Gamma_{g}, \tag{4}$$

$$\sigma \cdot \mathbf{n} = \mathbf{h}, \ \mathbf{x} \in \Gamma_h, \tag{5}$$

and initial conditions

$$\mathbf{u}(t=0) = \mathbf{u}_0,\tag{6}$$

$$p(t=0) = p_0,$$
 (7)

with position vector \mathbf{x} , time t, density ρ , velocity \mathbf{u} , Cauchy stress tensor σ , pressure p, dynamic viscosity μ , body force \mathbf{f} , which we assume to be zero, and surface normal vector \mathbf{n} . Eq. (4) is a Dirichlet boundary condition with prescribed velocity \mathbf{g} on Γ_g . Similarly,

Eq. (5) is a Neumann boundary condition with prescribed traction **h** on Γ_h . We may write these equations in abstract form as

$$\begin{cases} \mathcal{P}^{3D,fluid}(\mathbf{u}, p, \mathbf{x}, t) = \mathbf{0}, \\ \text{Boundary conditions,} \end{cases}$$
Initial conditions (8)

Following [19], these equations are discretized in space using a stabilized (variational multiscale) finite element formulation and in time using the generalized- α method. This yields the nonlinear residual equation at timestep n + 1

$$\mathbf{R}^{3D,fluid}(\dot{\mathbf{U}}_{n+1},\boldsymbol{\Pi}_{n+1}) = \mathbf{0},\tag{9}$$

to be solved for $\dot{\mathbf{U}}_{n+1}$ and $\mathbf{\Pi}_{n+1}$, the vectors of nodal accelerations and nodal pressures at the next timestep n+1, respectively. The residual is also a function of $\dot{\mathbf{U}}_n$ and $\mathbf{\Pi}_n$, but these are assumed to be known, and thus we do not explicitly write the functional dependence on them. This equation is solved using Newton's method, which in turn requires solving the following linear system at each Newton iteration k

$$\begin{bmatrix} \tilde{\mathbf{K}} & \mathbf{G} \\ \mathbf{D} & \mathbf{L} \end{bmatrix}_{n+1}^{(k)} \begin{bmatrix} \Delta \dot{\mathbf{U}}_{n+1}^{(k)} \\ \Delta \mathbf{\Pi}_{n+1}^{(k)} \end{bmatrix} = - \begin{bmatrix} \mathbf{R}_{m}^{3D,fluid} \\ \mathbf{R}_{c}^{3D,fluid} \end{bmatrix}_{n+1}^{(k)}.$$
(10)

 $\mathbf{R}_{m}^{3D,fluid}$ is the residual associated with momentum balance Eq. (1), while $\mathbf{R}_{c}^{3D,fluid}$ is the residual associated with mass continuity Eq. (2). $\tilde{\mathbf{K}},\mathbf{G},\mathbf{D},\mathbf{L}$ are blocks of the tangent or stiffness matrix, and $\Delta\dot{\mathbf{U}}_{n+1}^{(k)}$ and $\Delta\boldsymbol{\Pi}_{n+1}^{(k)}$ are the Newton increments in nodal accelerations and pressures, respectively. The notation $\left[\cdot\right]_{n+1}^{(k)}$ indicates that terms inside the brackets are evaluated at $\dot{\mathbf{U}}_{n+1}^{(k)}$ and $\boldsymbol{\Pi}_{n+1}^{(k)}$. The solutions are updated each Newton iteration until convergence according to

$$\dot{\mathbf{U}}_{n+1}^{(k+1)} = \dot{\mathbf{U}}_{n+1}^{(k)} + \Delta \dot{\mathbf{U}}_{n+1}^{(k)},\tag{11}$$

$$\Pi_{n+1}^{(k+1)} = \Pi_{n+1}^{(k)} + \Delta \Pi_{n+1}^{(k)}.$$
(12)

In cardiovascular biomechanics modeling, we are not only interested in blood flow, but also in the dynamics of the tissues surrounding the blood, notably the heart (Fig. 1 right). The deformation of these tissues is governed by the equations of finite deformation elastodynamics. Specifically, we may state the Cauchy momentum equation in Lagrangian form

$$\rho \frac{D\mathbf{u}}{Dt} - \nabla \cdot \boldsymbol{\sigma} - \mathbf{f} = \mathbf{0},\tag{13}$$

where $\frac{D}{Dt}$ denotes the material derivative. As with the fluid equations, \mathbf{u} is the velocity, $\boldsymbol{\sigma}$ is the Cauchy stress tensor, and \mathbf{f} is a body force, which we assume to be zero in this work. In our finite element solver, the structural problem is solved in the reference configuration, in which the relevant stress measure is the second Piola–Kirchhoff stress

$$S = JF^{-1}\sigma F^{-T}.$$
(14)

where **F** is the deformation gradient tensor and $J = \det \mathbf{F}$ is the Jacobian. For a hyperelastic material described by a strain energy density function $\psi(\mathbf{F})$, we have

$$S = \frac{\partial \psi}{\partial E},\tag{15}$$

where $\mathbf{E} = \frac{1}{2}(\mathbf{C} - \mathbf{I})$ is the Green-Lagrange strain tensor and $\mathbf{C} = \mathbf{F}^T \mathbf{F}$ is the right Cauchy-Green tensor. These equations are augmented with boundary and initial conditions so that we may write the structural dynamics problem in abstract form

$$\begin{cases} \mathcal{P}^{3D,struct}(\mathbf{u},\mathbf{x},t) = \mathbf{0}, \\ \text{Boundary conditions,} \\ \text{Initial conditions.} \end{cases} \tag{16}$$

These equations are solved using similar methods to those for fluid flow (i.e., finite element method and generalized- α method) [20], leading to an analogous nonlinear system of equations to be solved at each timestep

$$\mathbf{R}^{3D,struct}(\dot{\mathbf{U}}_{n+1}) = \mathbf{0}. \tag{17}$$

Usually, nodal displacements are chosen as the structural unknowns after time discretization, but in our implementation, we instead choose nodal accelerations. This is an arbitrary choice that allows the structure problem to be treated similarly to the fluid problem, but it is not necessary for the present coupling framework. The system is solved using Newton's method,

$$\left[\mathbf{K}\right]_{n+1}^{(k)} \left[\Delta \dot{\mathbf{U}}_{n+1}^{(k)} \right] = -\left[\mathbf{R}^{3D,struct} \right]_{n+1}^{(k)}, \tag{18}$$

where k again indicates the Newton iteration.

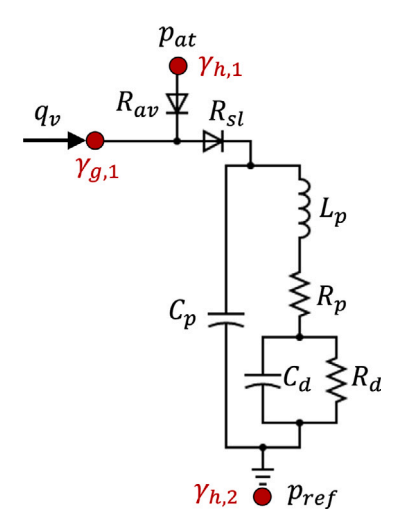


Fig. 2. An example of a 0D circulation model or LPN, which treats blood flow through the body like the flow of current through an electrical circuit. The LPN is forced by prescribed flowrates \mathbf{q} at the Dirichlet boundary nodes $\gamma_g = \{\gamma_{g,1}\}$ and prescribed pressures \mathbf{p} at the Neumann boundary nodes $\gamma_h = \{\gamma_{h,1}, \gamma_{h,2}\}$, both of which are denoted by red circles. (For interpretation of the references to color in this figure legend, the reader is referred to the web version of this article.)

In the remainder of the paper, we consider the general 3D problem

$$\begin{cases} \mathcal{P}^{3D}(\boldsymbol{\phi}, \mathbf{x}, t) = \mathbf{0}, \\ \text{Boundary conditions,} \\ \text{Initial conditions,} \end{cases}$$
 (19)

where \mathcal{P}^{3D} may represent either the 3D fluid or 3D structure PDE. ϕ are the 3D variables, which include velocity or velocity and pressure, depending on the physics. After space–time discretization, we obtain the general 3D residual equation as

$$\mathbf{R}^{3D}(\mathbf{\Phi}_{n+1}) = \mathbf{0}.\tag{20}$$

 Φ_{n+1} is the state vector of the 3D system, where, for the fluid, $\Phi_{n+1} = \begin{bmatrix} \dot{\mathbf{U}}_{n+1} \\ \mathbf{\Pi}_{n+1} \end{bmatrix}$, while for the structure, $\Phi_{n+1} = \dot{\mathbf{U}}_{n+1}$. Newton's method to solve this nonlinear system gives the general 3D linear system

$$\left[\frac{\partial \mathbf{R}^{3D}}{\partial \mathbf{\Phi}_{n+1}}\right]_{n+1}^{(k)} \left[\Delta \mathbf{\Phi}_{n+1}^{(k)}\right] = -\left[\mathbf{R}^{3D}\right]_{n+1}^{(k)}. \tag{21}$$

2.2. OD circulation model

Blood flow throughout the circulatory system is modeled using an LPN [20–22], also called a 0D fluid model. Fig. 2 shows an example LPN that will be used later in Section 3.1. LPN models are typically combinations of resistors R, which model the viscous resistance of vessels to blood flow, inductors L, which account for the inertia of blood, and capacitors C, which model the compliance of blood vessels. In addition, diodes are used to represent the heart valves. Many LPN models of the vasculature have been used in the literature, ranging from simple resistance or resistance—capacitance models of arteries to extensive closed-loop networks representing the entire circulatory system [19,22,36].

An LPN can be analyzed using Kirchhoff's first law for an electrical circuit, which leads to a general representation as a system of differential-algebraic equations (DAEs) [37],

$$\frac{d\mathbf{y}}{dt} = \mathbf{f}(\mathbf{y}, \mathbf{z}, t),\tag{22}$$

$$\mathbf{g}(\mathbf{y},\mathbf{z},t) = \mathbf{0},\tag{23}$$

with initial conditions

$$\mathbf{y}(t=0) = \mathbf{y}_0,\tag{24}$$

where y contains differential variables determined by the differential equations Eq. (22), z contains algebraic variables determined by the algebraic equations Eq. (23), and t is time. Both y and z contain pressures and flowrates at nodes and branches, respectively, and may also contain other variables, such as the cross-sectional area of a vessel or the state of a valve. f and g are potentially nonlinear functions of y, z, and t.

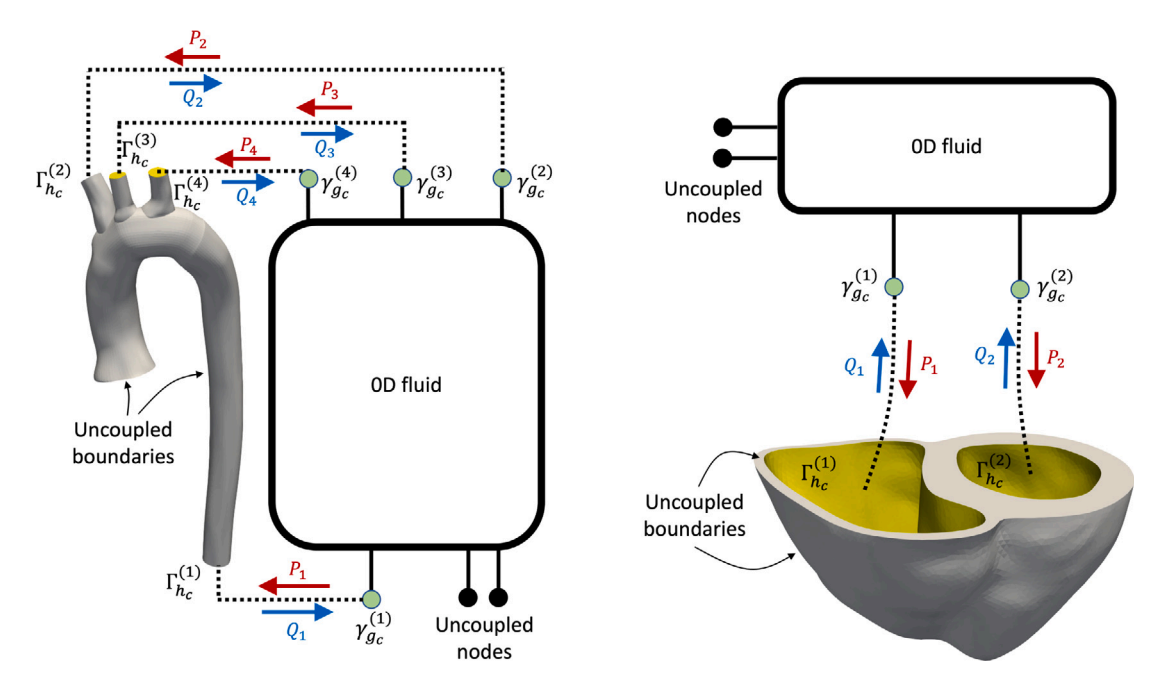


Fig. 3. Left: Coupling between a 3D fluid and 0D fluid. The 3D fluid is an aorta model taken from the Vascular Model Repository (https://www.vascularmodel.com/). Right: Coupling between a 3D structure and 0D fluid. The 3D structure is a biventricular model obtained from patient MRI data. Both coupling problems are treated identically. Coupled Neumann surfaces $\Gamma_{k_c}^{(i)}$ on the 3D models are highlighted in yellow. Coupled Dirichlet nodes $\gamma_{k_c}^{(i)}$ on the 0D model are shown in green. Along each $\Gamma_{k_c}^{(i)} - \gamma_{k_c}^{(i)}$ connection is an associated exchange of flowrate Q_i and pressure P_i . Note that in addition to coupled boundaries, the 3D model will generally have additional uncoupled boundaries on which one may prescribe uncoupled Dirichlet and/or Neumann boundary conditions, and likewise the 0D model will generally have additional uncoupled nodes on which one may prescribe uncoupled Dirichlet and/or Neumann boundary forcings. (For interpretation of the references to color in this figure legend, the reader is referred to the web version of this article.)

As with the 3D model, we may define boundary conditions for the 0D LPN model. Let γ_g denote the set of Dirichlet boundary nodes on which we prescribe flowrates **q**. Let γ_h denote the set of Neumann boundary nodes on which we prescribe pressures **p**. In Fig. 2, these boundary nodes are shown in red. The boundary flowrates and pressures are not boundary conditions in a strict sense because there is no notion of length in a 0D fluid model. Instead, they act as forcing terms directly in the 0D equations [17]

$$\frac{d\mathbf{y}}{dt} = \mathbf{f}(\mathbf{y}, \mathbf{z}, t, \mathbf{q}, \mathbf{p}),\tag{25}$$

$$\mathbf{g}(\mathbf{y}, \mathbf{z}, t, \mathbf{q}, \mathbf{p}) = \mathbf{0}. \tag{26}$$

y and z can often be considered together, so we define the combined 0D state vector $\mathbf{w} = [\mathbf{y}, \mathbf{z}]^T$. Analogous to the 3D system, the 0D equations are written in the following abstract form

$$\begin{cases} \mathcal{P}^{0D}(\mathbf{w}, t, \mathbf{q}, \mathbf{p}) = \mathbf{0}, \\ \text{Initial conditions.} \end{cases}$$
 (27)

In this work, we integrate the 0D system with a 4th-order Runge–Kutta (RK4) scheme (Appendix A). We first apply RK4 to integrate the differential variables \mathbf{y} using Eq. (25) from timestep n to n+1, then determine the algebraic variables \mathbf{z} with Eq. (26) using the updated differential variables. This yields a system of algebraic equations to be solved at timestep n+1

$$\mathbf{R}^{0D}(\mathbf{w}_{n+1}) = \mathbf{0}. \tag{28}$$

If the time-stepping scheme is explicit, as in this work, this system can be solved directly (i.e., in one iteration). If the scheme is implicit and the DAE system is nonlinear in w, this system can be solved by Newton's method.

2.3. The coupled problem

So far, we have individually discussed the numerical treatment of the 3D mechanical model and the 0D circulation model. In this section, we describe how these two models are mathematically coupled.

The 3D Neumann boundary is split into coupled and uncoupled parts, $\Gamma_h = \Gamma_{h_c} \cup \Gamma_{h_u}$. In general, there may be multiple distinct coupled Neumann boundaries, so that $\Gamma_{h_c} = \Gamma_{h_c}^{(1)} \cup \Gamma_{h_c}^{(2)} \cup \cdots \cup \Gamma_{h_c}^{(n^cB^c)}$, where n^{cBC} is the number of coupled boundaries. In Fig. 3, these are the outflow boundaries of the aorta model and the endocardial surfaces of the biventricular model (i.e., the inner surfaces

of the heart muscle in contact with the blood). Similarly, the set of 0D Dirichlet nodes is split into coupled and uncoupled parts, $\gamma_g = \gamma_{g_c} \cup \gamma_{g_d}$. The set of coupled Dirichlet nodes may be written $\gamma_{g_c} = \gamma_{g_c}^{(1)} \cup \gamma_{g_c}^{(2)} \cup \cdots \cup \gamma_{g_c}^{(n^cB^C)}$. Each 0D coupled Dirichlet node $\gamma_{g_c}^{(i)}$ is associated with a 3D coupled Neumann boundary $\Gamma_{h_c}^{(i)}$, $i \in \{1, \dots, n^{cBC}\}$, as shown in Fig. 3.

With these definitions in place, we may state the mathematical coupling between the 3D and 0D domains. For the 3D, we impose a spatially uniform pressure P_i on the coupled 3D boundary $\Gamma_{h_c}^{(i)}$, where the value of P_i is taken as the pressure at the corresponding coupled node $\gamma_{g_c}^{(i)}$ of the 0D model. Stated mathematically,

$$P_i = (\mathbb{P}\mathbf{w})_i$$
 on $\Gamma_h^{(i)}$, (29)

where \mathbb{P} is a matrix that selects the appropriate components from w. For example, if w has 5 components, but only the second and fourth components represent pressures at coupled nodes 1 and 2, then

$$\mathbb{P} = \begin{bmatrix} 0 & 1 & 0 & 0 & 0 \\ 0 & 0 & 0 & 1 & 0 \end{bmatrix}. \tag{30}$$

Note that the spatially uniform pressure assumption is made in several other coupling approaches [20-22].

Analogously, for the 0D, we impose a flowrate Q_i at the coupled 0D node $\gamma_{g_c}^{(i)}$, where the value of Q_i is taken as the velocity flux through the corresponding coupled boundary $\Gamma_{h}^{(i)}$ of the 3D model. Stated mathematically,

$$Q_i = \int_{\Gamma_b^{(i)}} \mathbf{u} \cdot \mathbf{n} d\Gamma \quad \text{at } \gamma_{g_c}^{(i)}, \tag{31}$$

where **n** is the outward surface normal vector. This definition of flowrate should be clear in the context of a 3D fluid. For a 3D structure, however, in order to define a flowrate Q_i , we must restrict our attention to 3D structures that enclose some volume of blood V_i , most commonly a chamber of the heart. Then, we may define flowrate as $Q_i = -\frac{dV_i}{dt}$. In Appendix B, using the Reynolds Transport Theorem, it is shown that Eq. (31) is equally valid for such a 3D structure, provided $\Gamma_{h_c}^{(i)}$ is a surface that closes the volume of interest V_i (see Section 2.6 if surface is not closed) and the integral is taken over $\Gamma_{h_c}^{(i)}$ in the deformed configuration. It is this observation that permits uniform treatment of 3D fluid and structure.

On a practical note, in the finite element setting, the flowrate integral is computed from the 3D degrees of freedom as follows.

$$Q_i = \int_{\Gamma_{h_c}^{(i)}} \mathbf{u} \cdot \mathbf{n} d\Gamma = \sum_A \int_{\Gamma_{h_c}^{(i)}} N_A(\mathbf{U})_A \cdot \mathbf{n} d\Gamma, \tag{32}$$

where $(U)_A$ is the velocity of node A of the finite element model and N_A is the associated shape function in the finite element formulation. Note also that in the time-discrete setting, the nodal velocities are obtained from the nodal accelerations by the generalized- α method expression

$$\mathbf{U}_{n+1} = \mathbf{U}_n + \Delta t \dot{\mathbf{U}}_n + \gamma \Delta t (\dot{\mathbf{U}}_{n+1} - \dot{\mathbf{U}}_n),\tag{33}$$

where Δt is the timestep size and γ is a parameter of the generalized- α method, not to be confused with the 0D Dirichlet and Neumann boundary node sets γ_g and γ_h . Recall that depending on the physical formulation (structure or fluid), $\dot{\mathbf{U}}$ is either precisely $\boldsymbol{\Phi}$ or a component of $\boldsymbol{\Phi}$.

The coupled problem in the time and space continuous domain may be summarized in the following abstract manner

$$\begin{cases} \mathcal{P}^{0D}(\mathbf{w},t,[\mathbf{q}_{u},\mathbf{Q}],\mathbf{p})=\mathbf{0}, \\ \text{Initial conditions,} \end{cases}$$
 Initial conditions,
$$\begin{cases} \mathcal{P}^{3D}(\boldsymbol{\phi},\mathbf{x},t)=\mathbf{0}, \\ \text{Initial conditions,} \end{cases}$$
 Uncoupled boundary conditions,
$$\sigma \cdot \mathbf{n}=-P_{i}\mathbf{n}, \text{ on } \Gamma_{h_{c}}^{(i)}, i \in \{1,\ldots,n^{cBC}\}, \end{cases}$$

$$P_{i}(t)=(\mathbb{P}\mathbf{w}(t))_{i}, \\ Q_{i}(t)=\int_{\Gamma_{h_{c}}^{(i)}(t)}\mathbf{u}(t)\cdot\mathbf{n}(t)d\Gamma, \end{cases}$$
 (34)

where the 0D Dirichlet forcing term \mathbf{q} is split into an uncoupled component \mathbf{q}_u , which are prescribed flowrates on the 0D model, and a coupled component \mathbf{Q} , which is obtained from the 3D model (i.e., $\mathbf{q} = [\mathbf{q}_u, \mathbf{Q}]$). Similarly, the 3D boundary conditions are split into an uncoupled component (Dirichlet or Neumann), which is prescribed, and coupled pressure boundary conditions with magnitude P_i , which are obtained from the 0D model. The expressions for P_i and Q_i , given in Eqs. (29) and (31) and restated here, provide the coupling conditions between 0D and 3D. While the values of the uncoupled boundary conditions for both 3D and 0D are generally prescribed, the values of the coupled pressure and flow boundary conditions, P_i and Q_i , are unknown and must be determined as part of the solution to the coupled problem.

After applying RK4 time discretization to the 0D system and applying generalized- α time discretization and finite element spatial discretization to the 3D system, the problem reduces to solving the following coupled nonlinear equations at each timestep n + 1,

$$\begin{cases}
\mathbf{R}^{0D}(\mathbf{w}_{n+1}, \mathbf{Q}_{n+1}(\mathbf{\Phi}_{n+1})) = \mathbf{0}, \\
\mathbf{R}^{3D}(\mathbf{\Phi}_{n+1}, \mathbf{P}_{n+1}(\mathbf{w}_{n+1})) = \mathbf{0},
\end{cases}$$
(35)

where, due to the coupling between 3D and 0D, the 0D residual \mathbf{R}^{0D} is a function of the 3D state vector $\mathbf{\Phi}_{n+1}$ through the interface flowrates \mathbf{Q}_{n+1} , and similarly the 3D residual \mathbf{R}^{3D} is a function of the 0D state vector \mathbf{w}_{n+1} through the interface pressures \mathbf{P}_{n+1} . The goal then is to find $\mathbf{\Phi}_{n+1}$ and \mathbf{w}_{n+1} that satisfy both 0D and 3D residual equations simultaneously. More to the point, the goal is to find *consistent* flowrates \mathbf{Q}_{n+1} and pressures \mathbf{P}_{n+1} , in the sense that \mathbf{Q}_{n+1} yields \mathbf{P}_{n+1} when solving the 0D system, and \mathbf{P}_{n+1} yields \mathbf{Q}_{n+1} when solving the 3D system.

2.4. Solving the coupled problem

The method to solve the system Eq. (35) is inspired by ANM [34], with modifications suggested in [38] and in [39]. The coupled problem is solved in a modular manner, which allows us to take advantage of codes that already exist to efficiently solve the 3D and 0D problems. Moreover, the 0D model may be modified without changing the 3D solver, and vice versa. Using ANM as a foundation, we reproduce the equations of the original coupling framework described in [19,35]. In addition, we show the equations apply not only to 3D fluid-0D fluid coupling, but also to 3D structure-0D fluid coupling.

It is instructive to first consider other potential approaches to solving Eq. (35). One option is to solve the 0D and 3D equations separately in a time-staggered fashion, for example

$$\begin{cases} \mathbf{R}^{0D}(\mathbf{w}_{n+1},\mathbf{Q}_n(\mathbf{\Phi}_n)) = \mathbf{0}, \\ \mathbf{R}^{3D}(\mathbf{\Phi}_{n+1},\mathbf{P}_{n+1}(\mathbf{w}_{n+1})) = \mathbf{0}, \end{cases}$$

or

$$\begin{cases} \mathbf{R}^{3D}(\boldsymbol{\Phi}_{n+1},\mathbf{P}_{n}(\mathbf{w}_{n})) = \mathbf{0}, \\ \mathbf{R}^{0D}(\mathbf{w}_{n+1},\mathbf{Q}_{n+1}(\boldsymbol{\Phi}_{n+1})) = \mathbf{0}. \end{cases}$$

These are analogous to the staggered schemes discussed in [29]. This approach has the advantage that within a timestep, each equation will have minimal convergence issues, since as far as each solver is concerned, the information from the other solver may be treated as a prescribed boundary condition. However, modifying the original equations incurs a splitting error, possibly leading to unphysical oscillations in time [29].

To solve the original Eq. (35), we may apply the same idea, but iterate it multiple times per timestep, for example,

$$\begin{cases} \mathbf{R}^{0D}(\mathbf{w}_{n+1}^{(k+1)}, \mathbf{Q}_{n+1}^{(k)}(\boldsymbol{\Phi}_{n+1}^{(k)})) = \mathbf{0}, \\ \mathbf{R}^{3D}(\boldsymbol{\Phi}_{n+1}^{(k+1)}, \mathbf{P}_{n+1}^{(k+1)}(\mathbf{w}_{n+1}^{(k+1)})) = \mathbf{0}, \end{cases}$$

where k is an iteration counter. This is a so-called nonlinear Gauss–Seidel iteration [40]. With this approach, one is solving the original equations, but there is no guarantee that the iteration will converge. In fact, in the particular application of coupling 3D heart models to 0D circulation models, this simple iteration will typically *diverge* during the isovolumic phases of the cardiac cycle, precisely due to the balloon dilemma. To illustrate this, we consider the situation where $\mathbf{Q}_{n+1}^{(k)}$ and $\mathbf{P}_{n+1}^{(k)}$ are scalars $\mathbf{Q}_{n+1}^{(k)}$ and $\mathbf{P}_{n+1}^{(k)}$ and one coupled boundary and node). Suppose the initial guess $\mathbf{Q}_{n+1}^{(0)}$ is slightly smaller than its converged value, which is near-zero since the cardiac valves are closed during the isovolumic phases. Because the closed valves have extremely high resistance \mathbf{R} , solving the \mathbf{R}^{0D} equation for $\mathbf{w}_{n+1}^{(1)}$ yields $\mathbf{P}_{n+1}^{(1)}$ which has roughly \mathbf{R} times the initial error in $\mathbf{Q}_{n+1}^{(0)}$. Then, solving the \mathbf{R}^{3D} for $\mathbf{\Phi}_{n+1}^{(1)}$ using $\mathbf{P}_{n+1}^{(1)}$ produces a $\mathbf{Q}_{n+1}^{(1)}$ which may have worse error than $\mathbf{Q}_{n+1}^{(0)}$, if \mathbf{R} is large enough. The process then repeats, leading to divergence of the iteration. Indeed, a variation of our coupling scheme which is nearly identical to the nonlinear Gauss–Seidel scheme was found to be unstable in our cardiac mechanics test case. This is discussed further in Section 4.

To avoid the balloon dilemma and improve convergence, one can apply Newton's method to solve Eq. (35), which yields a linear system to be solved at each Newton iteration, k,

$$\begin{bmatrix} \frac{\partial \mathbf{R}^{0D}}{\partial \mathbf{w}_{n+1}} & \frac{\partial \mathbf{R}^{0D}}{\partial \mathbf{\Phi}_{n+1}} \\ \frac{\partial \mathbf{R}^{3D}}{\partial \mathbf{w}_{n+1}} & \frac{\partial \mathbf{R}^{3D}}{\partial \mathbf{\Phi}_{n+1}} \end{bmatrix}_{n+1}^{(k)} \begin{bmatrix} \Delta \mathbf{w}_{n+1}^{(k)} \\ \Delta \mathbf{\Phi}_{n+1}^{(k)} \end{bmatrix} = - \begin{bmatrix} \mathbf{R}^{0D} \\ \mathbf{R}^{3D} \end{bmatrix}_{n+1}^{(k)},$$
(36)

with the update

$$\mathbf{\Phi}_{n+1}^{(k+1)} = \mathbf{\Phi}_{n+1}^{(k)} + \Delta \mathbf{\Phi}_{n+1}^{(k)} \quad \text{and} \quad \mathbf{w}_{n+1}^{(k+1)} = \mathbf{w}_{n+1}^{(k)} + \Delta \mathbf{w}_{n+1}^{(k)}. \tag{37}$$

As before, the notation $\left[\cdot\right]_{n+1}^{(k)}$ indicates that terms inside the brackets are evaluated at $\Phi_{n+1}^{(k)}$ and $\mathbf{w}_{n+1}^{(k)}$. This is identical to the monolithic approach of [20]. Conceptually, there is no balloon dilemma because there is no alternating iteration between 3D and 0D. The balloon dilemma can also be avoided by computing the resistance $(d\mathbf{P}/d\mathbf{Q})$ seen by the 3D model due to the 0D fluid and incorporating this information into the 3D solver. This is effective because the 3D residual depends not only *directly* on the 3D

variables Φ_{n+1} , but also indirectly on Φ_{n+1} through the flowrate-pressure relationship due to the 0D system. By providing the effect of flowrate on pressure to the 3D solver, it will choose an updated iterate of Φ_{n+1} that reduces the 3D residual, taking into account both the direct and indirect dependences. As we will show in the remainder of this section, these two approaches are essentially equivalent; that is, a manipulation of Newton's method leads to a coupling algorithm that demands a modification of the 3D solver to account for 0D resistance.

Having considered other approaches, we now proceed with our solution approach. Performing Schur Complement Reduction [41] (also known as Block Gauss Elimination or Static Condensation) on Eq. (36) yields the equivalent system

$$\begin{bmatrix} \frac{\partial \mathbf{R}^{0D}}{\partial \mathbf{w}_{n+1}} & \frac{\partial \mathbf{R}^{0D}}{\partial \mathbf{\Phi}_{n+1}} \\ \mathbf{0} & \frac{\partial \mathbf{R}^{3D}}{\partial \mathbf{\Phi}_{n+1}} - \frac{\partial \mathbf{R}^{3D}}{\partial \mathbf{w}_{n+1}} \left(\frac{\partial \mathbf{R}^{0D}}{\partial \mathbf{w}_{n+1}} \right)^{-1} \frac{\partial \mathbf{R}^{0D}}{\partial \mathbf{\Phi}_{n+1}} \end{bmatrix}_{n+1}^{(k)} \begin{bmatrix} \Delta \mathbf{w}_{n+1}^{(k)} \\ \Delta \mathbf{\Phi}_{n+1}^{(k)} \end{bmatrix} = - \begin{bmatrix} \mathbf{R}^{0D} \\ \mathbf{R}^{3D} - \frac{\partial \mathbf{R}^{3D}}{\partial \mathbf{w}_{n+1}} \left(\frac{\partial \mathbf{R}^{0D}}{\partial \mathbf{w}_{n+1}} \right)^{-1} \mathbf{R}^{0D} \end{bmatrix}_{n+1}^{(k)}.$$
(38)

From this, $\Delta\Phi_{n+1}^{(k)}$ can be determined by solving the linear system from the bottom row

$$\left[\frac{\partial \mathbf{R}^{3D}}{\partial \mathbf{\Phi}_{n+1}} - \frac{\partial \mathbf{R}^{3D}}{\partial \mathbf{w}_{n+1}} \left(\frac{\partial \mathbf{R}^{0D}}{\partial \mathbf{w}_{n+1}}\right)^{-1} \frac{\partial \mathbf{R}^{0D}}{\partial \mathbf{\Phi}_{n+1}}\right]_{n+1}^{(k)} \Delta \mathbf{\Phi}_{n+1}^{(k)} = -\left[\mathbf{R}^{3D} - \frac{\partial \mathbf{R}^{3D}}{\partial \mathbf{w}_{n+1}} \left(\frac{\partial \mathbf{R}^{0D}}{\partial \mathbf{w}_{n+1}}\right)^{-1} \mathbf{R}^{0D}\right]_{n+1}^{(k)}.$$
(39)

This is identical to the linear system for the uncoupled 3D problem Eq. (21), except for additional contributions to the 3D model's residual and tangent from the 0D model. For convenience, we denote the 0D contribution to the 3D tangent $\mathbf{K}^{3D/0D}$, where

$$\left[\mathbf{K}^{3D/0D}\right]_{n+1}^{(k)} = -\left[\frac{\partial \mathbf{R}^{3D}}{\partial \mathbf{w}_{n+1}} \left(\frac{\partial \mathbf{R}^{0D}}{\partial \mathbf{w}_{n+1}}\right)^{-1} \frac{\partial \mathbf{R}^{0D}}{\partial \Phi_{n+1}}\right]_{n+1}^{(k)}.\tag{40}$$

As will be shown, rather than considering the 0D contribution to the 3D residual, it is more convenient to consider the entire 0D-modified 3D residual $\mathbf{R}^{3D/0D}$, where

$$\left[\mathbf{R}^{3D/0D}\right]_{n+1}^{(k)} = \left[\mathbf{R}^{3D} - \frac{\partial \mathbf{R}^{3D}}{\partial \mathbf{w}_{n+1}} \left(\frac{\partial \mathbf{R}^{0D}}{\partial \mathbf{w}_{n+1}}\right)^{-1} \mathbf{R}^{0D}\right]_{n+1}^{(k)}.$$
(41)

Thus, the solution strategy is as follows:

- 1. Approximate $[\mathbf{R}^{3D/0D}]_{n+1}^{(k)}$. 2. Approximate $[\mathbf{K}^{3D/0D}]_{n+1}^{(k)}$.
- 3. Solve the modified 3D linear system

$$\left[\frac{\partial \mathbf{R}^{3D}}{\partial \Phi_{n+1}} + \mathbf{K}^{3D/0D}\right]^{(k)} \Delta \Phi_{n+1}^{(k)} = -\left[\mathbf{R}^{3D/0D}\right]^{(k)}_{n+1}.$$
(42)

We then perform the Newton update with $\Delta\Phi_{n+1}^{(k)}$, proceed to the next Newton iteration k+1, and repeat until convergence. Note that because we use RK4 (an explicit scheme) for the 0D system, the 0D system does not depend on an updated guess for \mathbf{w}_{n+1} , and thus we do not need to compute $\Delta \mathbf{w}_{n,1}^{(k)}$

The approximations for $\left[\mathbf{R}^{3D/0D}\right]_{n+1}^{(k)}$ and $\left[\mathbf{K}^{3D/0D}\right]_{n+1}^{(k)}$ are performed using a fixed point iteration operator $F^{0D}(\mathbf{w}_{n+1}, \mathbf{\Phi}_{n+1})$ for the 0D system, which is introduced next. Then, explicit expressions for the two terms are provided.

2.4.1. 0D fixed point iteration operator

Here, we introduce the 0D fixed point iteration operator, which is necessary for the 0D residual and tangent approximations to follow. Assume we have an operator $F^{0D}(\mathbf{w}_{n+1}, \Phi_{n+1})$ such that the iteration $\mathbf{w}_{n+1}^{(m+1)} = F^{0D}(\mathbf{w}_{n+1}^{(m)}, \Phi_{n+1})$ converges to the solution of $\mathbf{R}^{0D}(\mathbf{w}_{n+1}, \Phi_{n+1}) = \mathbf{0}$ (for fixed Φ_{n+1}). One can identify this operator for nearly all conceivable 0D solvers, implicit or explicit. In this work, RK4 is used to integrate the 0D system, and the fixed point operator corresponding to RK4, $F^{0D.RK4}(\mathbf{w}_{n+1}, \Phi_{n+1})$, is provided in Appendix A. As was done for \mathbf{R}^{0D} (Eq. (35)), it is convenient to view F^{0D} as a function of Φ_{n+1} through the coupling flowrates \mathbf{Q}_{n+1} as,

$$F^{0D}(\mathbf{w}_{n+1}, \mathbf{\Phi}_{n+1}) = F^{0D}(\mathbf{w}_{n+1}, \mathbf{Q}_{n+1}(\mathbf{\Phi}_{n+1})). \tag{43}$$

We briefly list some relevant features of $F^{0D,RK4}$. Because RK4 is an explicit scheme, $F^{0D,RK4}$ is a function of Φ_{n+1} , but is not a function of \mathbf{w}_{n+1} . However, for generality and in case one is interested in using an implicit scheme, we retain its dependence on \mathbf{w}_{n+1} in the remainder of the derivation. It is a fixed point operator corresponding to Newton's method, which converges in one iteration; in other words, $\mathbf{w}_{n+1}^{(m+1)} = F^{0D,RK4}(\mathbf{w}_{n+1}^{(m)}, \mathbf{Q}_{n+1}(\Phi_{n+1}))$ converges to the solution of $\mathbf{R}^{0D}(\mathbf{w}_{n+1}, \mathbf{Q}_{n+1}(\Phi_{n+1})) = \mathbf{0}$ in only one step regardless of $\mathbf{w}_{n+1}^{(m)}$. Finally, on a practical note, we emphasize that F^{0D} is also a function of \mathbf{w}_n and \mathbf{Q}_n , which are assumed to be known. See Appendix A for more details.

With F^{0D} described, we continue by deriving explicit expressions for $[\mathbf{R}^{3D/0D}]_{n+1}^{(k)}$ and $[\mathbf{K}^{3D/0D}]_{n+1}^{(k)}$

2.4.2. OD-modified 3D residual

In this section, an explicit expression is derived for $[\mathbf{R}^{3D/0D}]_{n=1}^{(k)}$. Recall Eq. (41),

$$\left[\mathbf{R}^{3D/0D}\right]_{n+1}^{(k)} = \left[\mathbf{R}^{3D} - \frac{\partial \mathbf{R}^{3D}}{\partial \mathbf{w}_{n+1}} \left(\frac{\partial \mathbf{R}^{0D}}{\partial \mathbf{w}_{n+1}}\right)^{-1} \mathbf{R}^{0D}\right]_{n+1}^{(k)}.$$

First, use a finite difference approximation as suggested in [39],

$$\left[\mathbf{R}^{3D/0D}\right]_{n+1}^{(k)} = \left[\mathbf{R}^{3D} - \frac{\partial \mathbf{R}^{3D}}{\partial \mathbf{w}_{n+1}} \left(\frac{\partial \mathbf{R}^{0D}}{\partial \mathbf{w}_{n+1}}\right)^{-1} \mathbf{R}^{0D}\right]_{n+1}^{(k)} \approx \mathbf{R}^{3D} (\mathbf{\Phi}_{n+1}^{(k)}, \tilde{\mathbf{w}}_{n+1}^{(k)}), \tag{44}$$

where

$$\tilde{\mathbf{w}}_{n+1}^{(k)} = \mathbf{w}_{n+1}^{(k)} - \left[\left(\frac{\partial \mathbf{R}^{0D}}{\partial \mathbf{w}_{n+1}} \right)^{-1} \mathbf{R}^{0D} \right]_{n+1}^{(k)}. \tag{45}$$

Note that in our case, the 3D residual \mathbf{R}^{3D} is linear in the 0D variables \mathbf{w}_{n+1} , so this approximation is exact. Eq. (45) is in fact one Newton iteration to solve the 0D system at fixed $\Phi_{n+1}^{(k)}$ (or $\mathbf{Q}_{n+1}^{(k)}$). Thus, we may approximate it using the 0D fixed point operator

$$\tilde{\mathbf{w}}_{n+1}^{(k)} \approx F^{0D}(\mathbf{w}_{n+1}^{(k)}, \mathbf{\Phi}_{n+1}^{(k)}).$$
 (46)

If F^{0D} is a Newton iteration, as in our case, this approximation is exact.

In terms of implementation, at each Newton iteration, first compute $\tilde{\mathbf{w}}_{n+1}^{(k)}$ using Eq. (46). Recalling \mathbf{R}^{3D} is a function of \mathbf{w}_{n+1} through coupling pressures (Eq. (35)), next compute modified pressures defined as

$$\tilde{\mathbf{P}}_{n+1}^{(k)} = \mathbb{P}\tilde{\mathbf{w}}_{n+1}^{(k)}.$$
(47)

Finally, evaluate

$$\left[\mathbf{R}^{3D/0D}\right]_{n+1}^{(k)} = \mathbf{R}^{3D}(\mathbf{\Phi}_{n+1}^{(k)}, \tilde{\mathbf{P}}_{n+1}^{(k)}). \tag{48}$$

This last step can be implemented as follows in a 3D finite element solver. Splitting the residual into a term from the coupled Neumann boundaries and terms from all other residual contributions (internal stresses, other boundary conditions, etc.), $\left[\mathbf{R}^{3D/0D}\right]_{n+1}^{(k)}$ is computed as follows:

$$\left(R^{3D/0D}\right)_{n+1,Ai}^{(k)} = \text{Uncoupled residual terms} + \sum_{m=1}^{n^{cBC}} \int_{\Gamma_{h_c}^{(m)}} N_A \tilde{P}_{n+1,m}^{(k)} n_i d\Gamma, \tag{49}$$

where A is the node index, i indexes the spatial dimension, m indexes the coupled Neumann boundaries, of which there are n^{cBC} , and $\Gamma_{h_c}^{(m)}$ is the surface corresponding to coupled Neumann boundary m. N_A is the shape function for node A, $\tilde{P}_{n+1,m}^{(k)}$ is the mth component of $\tilde{\mathbf{P}}_{n+1}^{(k)}$, and n_i is the ith component of the outward surface normal. The integral expression in Eq. (49) is the same as for any other (uncoupled) pressure boundary condition; the only difference is that the value of the pressure $\tilde{P}_{n+1,j}^{(k)}$ is obtained by communicating with the 0D solver. If \mathbf{R}^{3D} contains momentum and continuity components (as in the fluid system Eq. (10)), the contribution of the coupled Neumann boundary conditions should be assembled into the *momentum* equation residual.

Remark: We point out the minor difference in Eq. (49) when considering a 3D fluid–OD fluid problem vs. a 3D structure–OD fluid problem. For a 3D fluid, we may consider the fluid domain to be fixed (non-deforming), so the integral is taken over the coupled surface in the reference configuration. For a 3D structure, we typically assume a "follower pressure load." Thus, if the structure deforms, the integral is taken over the coupled surface in the current (deformed) configuration with the current surface normal vector, corresponding to timestep n + 1.

2.4.3. OD contribution to 3D tangent

In this section, an explicit expression is derived for $\left[\mathbf{K}^{3D/0D}\right]_{n+1}^{(k)}$. Recall Eq. (40),

$$\left[\mathbf{K}^{3D/0D}\right]_{n+1}^{(k)} = -\left[\frac{\partial \mathbf{R}^{3D}}{\partial \mathbf{w}_{n+1}} \left(\frac{\partial \mathbf{R}^{0D}}{\partial \mathbf{w}_{n+1}}\right)^{-1} \frac{\partial \mathbf{R}^{0D}}{\partial \mathbf{\Phi}_{n+1}}\right]_{n+1}^{(k)}.$$

Following [34], define a matrix C

$$\mathbf{C} = \left(\frac{\partial \mathbf{R}^{0D}}{\partial \mathbf{w}_{n+1}}\right)^{-1} \frac{\partial \mathbf{R}^{0D}}{\partial \Phi_{n+1}},\tag{50}$$

so that

$$\left[\mathbf{K}^{3D/0D}\right]_{n+1}^{(k)} = -\left[\frac{\partial \mathbf{R}^{3D}}{\partial \mathbf{w}_{n+1}}\mathbf{C}\right]_{n+1}^{(k)}.$$

The key approximation is provided in [34], in which it was shown that C can be reasonably approximated by

$$\mathbf{C} \approx -\frac{\partial F^{0D}(\mathbf{w}_{n+1}, \mathbf{\Phi}_{n+1})}{\partial \mathbf{\Phi}_{n+1}} = -\frac{\partial F^{0D}(\mathbf{w}_{n+1}, \mathbf{Q}_{n+1})}{\partial \mathbf{Q}_{n+1}} \frac{\partial \mathbf{Q}_{n+1}}{\partial \mathbf{U}_{n+1}} \frac{\partial \mathbf{U}_{n+1}}{\partial \mathbf{\Phi}_{n+1}}, \tag{51}$$

where we have used the chain rule and the fact that F^{0D} is a function of Φ_{n+1} through the flowrates \mathbf{Q}_{n+1} and the nodal velocities \mathbf{U}_{n+1} (Eqs. (32) and (33)).

 \mathbf{U}_{n+1} (Eqs. (32) and (33)). For the other term, $\frac{\partial \mathbf{R}^{3D}}{\partial \mathbf{w}_{n+1}}$, we also apply the chain rule and the fact that \mathbf{R}^{3D} is a function of \mathbf{w}_{n+1} through the pressures \mathbf{P}_{n+1} (Eq. (29))

$$\frac{\partial \mathbf{R}^{3D}}{\partial \mathbf{w}_{n+1}} = \frac{\partial \mathbf{R}^{3D}}{\partial \mathbf{P}_{n+1}} \frac{d\mathbf{P}_{n+1}}{d\mathbf{w}_{n+1}} = \frac{\partial \mathbf{R}^{3D}}{\partial \mathbf{P}_{n+1}} \mathbb{P}.$$
 (52)

Thus, the 0D tangent matrix contribution is

$$\left[\mathbf{K}^{3D/0D}\right]_{n+1}^{(k)} = \left[\frac{\partial \mathbf{R}^{3D}}{\partial \mathbf{P}_{n+1}} \mathbb{P} \frac{\partial F^{0D}(\mathbf{w}_{n+1}, \mathbf{Q}_{n+1})}{\partial \mathbf{Q}_{n+1}} \frac{\partial \mathbf{Q}_{n+1}}{\partial \mathbf{U}_{n+1}} \frac{\partial \mathbf{U}_{n+1}}{\partial \mathbf{\Phi}_{n+1}}\right]_{n+1}^{(k)}.$$
(53)

All partial derivatives are computed analytically (see Appendix C for details) except for

$$\left[\mathbb{P}\frac{\partial F^{0D}(\mathbf{w}_{n+1},\mathbf{Q}_{n+1})}{\partial \mathbf{Q}_{n+1}}\right]_{n+1}^{(k)}.$$

This term, which is denoted by M, is computed in a finite difference manner by communicating with the 0D solver as

$$M_{ij} = \left[\mathbb{P}_{ip} \left(\frac{\partial F^{0D}(\mathbf{w}_{n+1}, \mathbf{Q}_{n+1})}{\partial \mathbf{Q}_{n+1}} \right)_{pj} \right]_{n+1}^{(k)}$$

$$\approx \frac{\mathbb{P}_{ip} F_p^{0D}(\mathbf{w}_{n+1}^{(k)}, \mathbf{Q}_{n+1}^{(k)} + \epsilon \mathbf{e}_j) - \mathbb{P}_{ip} F_p^{0D}(\mathbf{w}_{n+1}^{(k)}, \mathbf{Q}_{n+1}^{(k)})}{\epsilon}.$$

where \mathbf{e}_j is the jth unit vector and ϵ is a small numerical perturbation. Note that for the evaluation of $\left[\mathbf{R}^{3D/0D}\right]_{n+1}^{(k)}$, we already require

$$\mathbb{P}F^{0D}(\mathbf{w}_{n+1}^{(k)}, \mathbf{Q}_{n+1}^{(k)}) = \mathbb{P}\tilde{\mathbf{w}}_{n+1}^{(k)} = \tilde{\mathbf{P}}_{n+1}^{(k)}.$$

The slightly perturbed quantity, $\mathbb{P}F^{0D}(\mathbf{w}_{n+1}^{(k)}, \mathbf{Q}_{n+1}^{(k)} + \epsilon \mathbf{e}_j)$, can be computed in exactly the same manner. We define $\tilde{\mathbf{w}}_{n+1,\epsilon_j}^{(k)}$ and $\tilde{\mathbf{P}}_{n+1,\epsilon_j}^{(k)}$ such that

$$\mathbb{P}F^{0D}(\mathbf{w}_{n+1}^{(k)},\mathbf{Q}_{n+1}^{(k)}+\epsilon\mathbf{e}_j)=\mathbb{P}\tilde{\mathbf{w}}_{n+1,\epsilon_i}^{(k)}=\tilde{\mathbf{P}}_{n+1,\epsilon_i}^{(k)}.$$

Thus, we may write

$$M_{ij} = \frac{\tilde{P}_{n+1,\epsilon_j,i}^{(k)} - \tilde{P}_{n+1,i}^{(k)}}{\epsilon}.$$
 (54)

In this form, it is revealed that M_{ij} is a resistance matrix that describes how pressure at coupled node i changes with flowrate at coupled surface j. As indicated previously, we have shown that this manipulation of Newton's method demands a modification of the 3D solver to account for 0D resistance. Following [19], the off-diagonal entries of M_{ij} are ignored in this work. Since M_{ij} factors into the tangent but not the residual, ignoring the off-diagonal components affects the rate of convergence but not the converged solution itself, analogous to an inexact Newton method. In practice, we did not see convergence issues with this modification, which improves the sparsity of the tangent contribution and decreases the computational cost.

The resulting 0D tangent contribution is given as (again, see Appendix C for derivation)

$$\left(K^{3D/0D}\right)_{n+1,AiBj}^{(k)} = \sum_{l=1}^{n^{cBC}} \sum_{m=1}^{n^{cBC}} \gamma \Delta t M_{lm} \int_{\Gamma_{h_c}^{(l)}} N_A n_i d\Gamma \int_{\Gamma_{h_c}^{(m)}} N_B n_j d\Gamma.$$
 (55)

The variable definitions are the same as for $\mathbf{R}^{3D/0D}$ (a vector), with the addition of indices (B, j, m) since we are now dealing with a matrix. Analogous to the 0D-modified 3D residual, the 0D tangent contribution should be assembled into the *momentum–acceleration* block of the tangent matrix, if applicable.

Remark: For a 3D structure–0D fluid problem, the integrals in Eq. (55) should be taken over the coupled surface in the current (deformed) configuration with the current surface normal vector, corresponding to timestep n + 1.

Remark: Eq. (49) (0D-modified 3D residual) and Eq. (55) (0D contribution to the 3D tangent) can be found in [19,35], in slightly different notation. However, we obtain these expressions through a new derivation involving ANM and show that they apply not only to the 3D fluid–0D fluid problem, but also to the 3D structure–0D fluid problem.

2.4.4. Summary

The coupling strategy is summarized below. See Fig. 4 for a graphical representation of the required computations and communications. At each Newton iteration k,

1. Compute $\mathbf{Q}_{n+1}^{(k)} = f(\mathbf{\Phi}_{n+1}^{(k)})$, where f is some function according to Eqs. (32) and (33), and communicate with the 0D solver. The 3D solver must also compute and send $\mathbf{Q}_n = f(\mathbf{\Phi}_n)$, which is also required by the 0D solver (see Appendix A for more details).

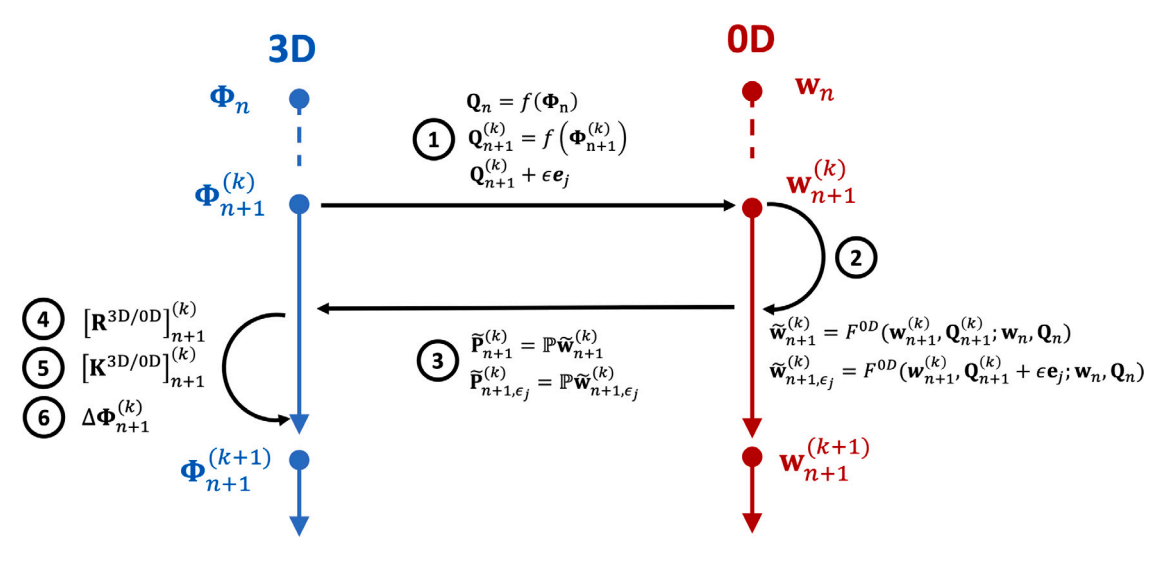


Fig. 4. Communication diagram between 3D and 0D solvers. At each timestep n, we iterate until convergence. At each Newton iteration k, we perform 6 computations/communications. These steps correspond to the coupling algorithm summary in Section 2.4.4.

2. Compute

$$\begin{split} & \tilde{\mathbf{w}}_{n+1}^{(k)} = F^{0D}(\mathbf{w}_{n+1}^{(k)}, \mathbf{Q}_{n+1}^{(k)}; \mathbf{w}_n, \mathbf{Q}_n), \\ & \tilde{\mathbf{w}}_{n+1, \epsilon_i}^{(k)} = F^{0D}(\mathbf{w}_{n+1}^{(k)}, \mathbf{Q}_{n+1}^{(k)} + \epsilon \mathbf{e}_j; \mathbf{w}_n, \mathbf{Q}_n), \quad j \in \{1, \dots, n^{cBc}\}. \end{split}$$

This requires $n^{cBc} + 1$ calls to the 0D solver.

3. Compute

$$\begin{split} \tilde{\mathbf{P}}_{n+1}^{(k)} &= \mathbb{P} \tilde{\mathbf{w}}_{n+1}^{(k)}, \\ \tilde{\mathbf{P}}_{n+1,\epsilon_i}^{(k)} &= \mathbb{P} \tilde{\mathbf{w}}_{n+1,\epsilon_i}^{(k)}, \quad j \in \{1,\dots,n^{cBc}\}. \end{split}$$

This requires the 0D to simply extract the proper components of $\tilde{\mathbf{w}}_{n+1}^{(k)}$ and $\tilde{\mathbf{w}}_{n+1,\varepsilon_i}^{(k)}$ and send them to 3D.

- 4. Given $\tilde{\mathbf{P}}_{n+1}^{(k)}$, compute $\left[\mathbf{R}^{3D/0D}\right]_{n+1}^{(k)}$ using Eq. (49). 5. Given $\tilde{\mathbf{P}}_{n+1}^{(k)}$ and $\tilde{\mathbf{P}}_{n+1,\epsilon_{j}}^{(k)}$, $j \in \{1, \dots, n^{cBc}\}$, compute **M** using Eq. (54) and construct $\left[\mathbf{K}^{3D/0D}\right]_{n+1}^{(k)}$ using Eq. (55).
- 6. Solve the modified 3D linear system Eq. (42)

$$\left[\frac{\partial \mathbf{R}^{3D}}{\partial \mathbf{\Phi}_{n+1}} + \mathbf{K}^{3D/0D}\right]_{n+1}^{(k)} \Delta \mathbf{\Phi}_{n+1}^{(k)} = -\left[\mathbf{R}^{3D/0D}\right]_{n+1}^{(k)},$$

for $\Delta \Phi_{n+1}^{(k)}$.

The 3D degrees of freedom are updated with $\Delta\Phi_{n+1}^{(k)}$, the Newton iteration index is incremented $k \to k+1$, and the process repeats until $[\mathbf{R}^{3D/0D}]_{n+1}^{(k)}$ falls below a prescribed relative or absolute tolerance.

2.5. Numerical considerations

The OD tangent contribution $\left[\mathbf{K}^{3D/0D}\right]_{n+1}^{(k)}$ is dense and adding it explicitly to $\left[\frac{\partial \mathbf{R}^{3D}}{\partial \Phi_{n+1}}\right]_{n+1}^{(k)}$ may deteriorate the performance of the linear solver, which typically takes advantage of the sparse structure of tangent matrices arising in finite element solvers [42]. To address this, we rewrite Eq. (55) as

$$\left(K^{3D/0D}\right)_{n+1,AiB_{j}}^{(k)} = \sum_{l=1}^{n^{cBC}} \sum_{m=1}^{n^{cBC}} \gamma \Delta t M_{lm}(S_{l})_{Ai}(S_{m})_{Bj}, \quad (S_{l})_{Ai} = \int_{\Gamma_{h}^{(l)}} N_{A} n_{i} d\Gamma.$$
 (56)

That is, $\left[\mathbf{K}^{3D/0D}\right]_{n+1}^{(k)}$ is the sum of rank 1 matrices. It is more efficient to store the vector \mathbf{S}_l separately and apply when needed (in matrix multiplication and in preconditioning) than to explicitly form the outer product and add it to the tangent [35].

The 0D tangent contribution also increases the condition number of the linear system, proportional to the resistance of the coupled Neumann boundaries (i.e., M). This can cause poor performance of standard iterative linear solvers. Resistance-based preconditioning is an effective remedy [35,43].



Fig. 5. Left: An idealized LV. Right: The same model with a cap surface shown in red, which, combined with the endocardial surface, defines a closed surface with which to compute volume/flowrate. (For interpretation of the references to color in this figure legend, the reader is referred to the web version of this article.)

2.6. Capping non-closed surfaces and consequences

The proposed coupling method requires computing flowrates from the 3D domain. For a 3D structure, this flowrate is identical to the negative rate of change of the enclosed volume. An important complication arises if the structure does not enclose a volume, such as in cardiac modeling. When the cardiac valves are closed, each cardiac chamber encloses a volume. However, the valves are often ignored when modeling the heart. As an example, Fig. 5 (left) shows an idealized LV, where the inflow and outflow valves are omitted. Here, we would like to couple the endocardial surface to a 0D fluid model, but the endocardial surface is not closed. Not accounting for this will lead to an inaccurately computed flowrate. In this work, we address this issue by introducing a "cap," a surface that closes the endocardial surface, thereby defining an enclosed fluid-tight volume (Fig. 5 right). Stated formally, if a coupled surface $\Gamma_{h_c}^{(i)}$ is not closed, we consider a cap surface $\Gamma_{h_c,cap}^{(i)}$ such that $\Gamma_{h_c}^{(i)} \cup \Gamma_{h_c,cap}^{(i)}$ is a closed surface. Because there is some flexibility in defining the cap surface, in our formulation, we leave the responsibility of constructing it

Because there is some flexibility in defining the cap surface, in our formulation, we leave the responsibility of constructing it to the user. Methods exist for constructing such surfaces, such as the ear clipping algorithm [44] or the vtkFillHolesFilter from VTK [45], the latter being used in this work.

We note that this cap surface is used only for computing flowrate and should not be treated in the same manner as a boundary of the 3D model. In particular, even though the cap surface is used to compute flowrate, the coupling pressure is not applied to the cap surface. The consequences are as follows. When computing flowrates, the cap surface is included in the integral in Eq. (32),

$$Q_i = \sum_{A} \Big(\int_{\Gamma_{h_c}^{(i)}} N_A(\mathbf{U})_A \cdot \mathbf{n} d\, \Gamma + \int_{\Gamma_{h_c,cap}^{(i)}} N_A(\mathbf{U})_A \cdot \mathbf{n} d\, \Gamma \Big).$$

When computing the 0D-modified residual, the cap surface is not included in the pressure integral in Eq. (49); it is unchanged,

$$\left(R^{3D/0D}\right)_{n+1,Ai}^{(k)} = \text{Uncoupled residual terms} + \sum_{i=1}^{n^{cBC}} \int_{\Gamma_h^{(i)}} N_A \tilde{P}_{n+1,j}^{(k)} n_i d\Gamma.$$

When computing the 0D tangent contribution, the cap surface is ignored in the first integral, but included in the second integral in Eq. (55),

$$\left(K^{3D/0D}\right)_{n+1,AiBj}^{(k)} = \sum_{l=1}^{n^{cBC}} \sum_{m=1}^{n^{cBC}} \gamma \Delta t M_{lm} \int_{\varGamma_{h_c}^{(l)}} N_A n_i d\varGamma \Big(\int_{\varGamma_{h_c}^{(m)}} N_B n_j d\varGamma + \int_{\varGamma_{h_c,cap}^{(m)}} N_B n_j d\varGamma \Big).$$

Note that the cap surface is constructed once and evolved with the deformation of the model. Note also that the expressions above assume the cap surface does not introduce any new nodes in the interior of the surface. If the cap included interior nodes, we would have to interpolate velocities from the boundary nodes (where the velocity is well-defined) to these interior nodes, and the above expressions would have to account for this interpolation. We leave this problem for future work.

3. Results

The present coupling method is implemented in svFSI, a multiphysics finite element solver for cardiovascular modeling [30]. In the following sections, we demonstrate the coupling method in several illustrative and clinically relevant examples, as well as assess the convergence behavior and cost of our method.

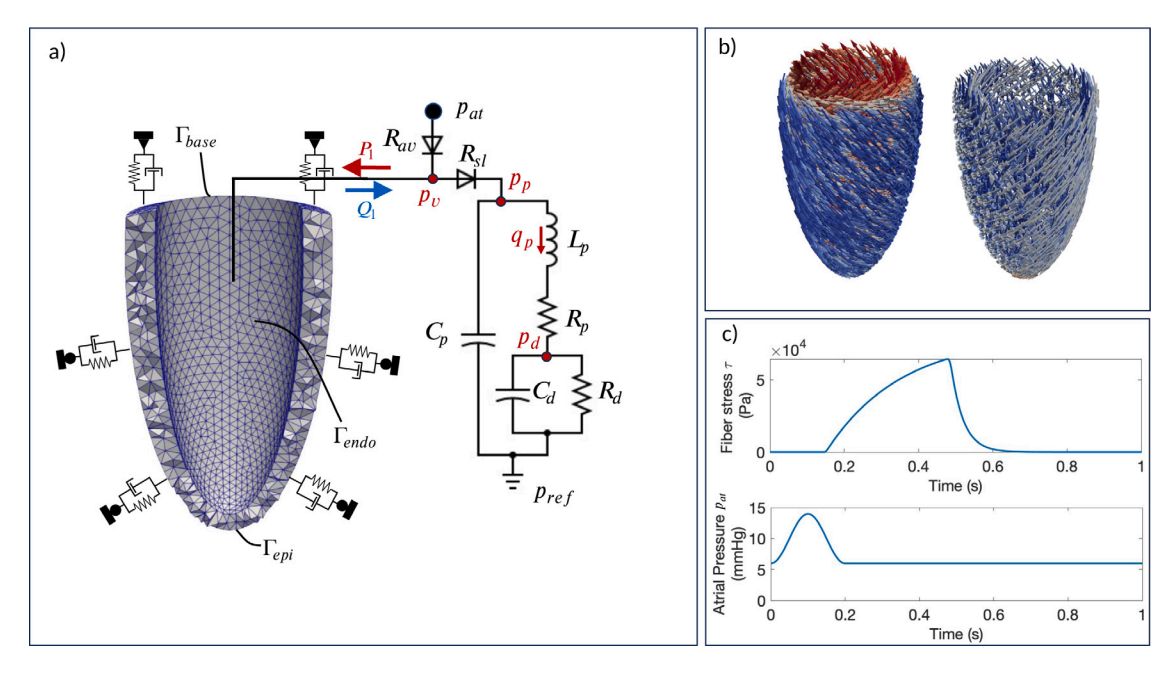


Fig. 6. Problem setup for the coupled idealized LV example. (a) An idealized LV model, shown in cut-view, is coupled to an open-loop LPN of the systemic circulation. The LV is supported by Robin boundary conditions (denoted by the spring–dashpot assemblies) on the base and epicardial surfaces, and periodic active stress along fiber directions causes the LV to contract. (b) Fiber **f** (left) and sheet s (right) orientation fields for the idealized LV model. Arrows denote the local fiber or sheet direction, and they are colored by their component along the longitudinal axis. Fiber angles (relative to circumferential) vary from $+60^{\circ}$ on the endocardial surface to -60° degrees on the epicardial surface. (c) Fiber stress curve (top) and prescribed atrial pressure curve (bottom). Here, we assume the cardiac cycle duration is 1s. Atrial systole is set to begin at $t_{sys,a} = 0$ ms and lasts for a duration $T_{sys,a} = 200$ ms. Atrial pressure ranges between 6 mmHg and 14 mmHg. Ventricular systole is set to begin at $t_{sys,a} = 143$ ms, and the active stress reaches a maximum value of approximately 65 kPa (488 mmHg). A complete list of simulation parameters is provided in Table 1. (For interpretation of the references to color in this figure legend, the reader is referred to the web version of this article.)

3.1. Idealized left ventricle with open-loop circulation

In this example, we simulate a LV with active contraction, pumping blood through an open-loop LPN model of the systemic circulation. The idealized LV geometry is that of a truncated, prolate ellipsoid [46] (Fig. 6a), with three surfaces: epicardial (outer) Γ_{epi} , endocardial (inner) Γ_{endo} , and basal (top) Γ_{base} . The geometry is meshed with linear tetrahedral elements with an average edge length of approximately 5 mm, yielding a mesh with 23,897 elements and 5,357 nodes (16,071 degrees of freedom). We also construct a fiber orientation field [46], which is used in a fiber-based constitutive model of the myocardium, described next. The fiber orientations $\bf f$ vary linearly from +60° (relative to circumferential) on the endocardial surface to -60° on the epicardial surface. The material model also requires a "sheet" orientation field $\bf s$, which in this work is perpendicular to $\bf f$ and to the ellipsoidal normal direction $\bf n$. See Fig. 6b for visualization.

The myocardium is modeled with a Holzapfel–Ogden strain energy, plus a quadratic volumetric penalty term. In addition, we include a viscous pseudo-potential, which accounts for viscous dissipation in the collagen and elastin matrix surrounding muscle fibers [47,48], and an active stress term, which acts along fiber directions to recapitulate cardiac contraction [48,49]. The second Piola–Kirchhoff stress is thus given by

$$\mathbf{S} = \frac{\partial}{\partial \mathbf{E}} (\psi_{HO} + \psi_{vol}) + \frac{\partial}{\partial \dot{\mathbf{E}}} (\psi_{visc}) + \mathbf{S}_{act}, \tag{57}$$

$$\psi_{HO} = \frac{a}{2b} \left(e^{b(\bar{I}_1 - 3)} - 1 \right) + \frac{a_{fs}}{2b_{fs}} \left(e^{b_{fs}I_{8,fs}^2} - 1 \right) + \sum_{i \in \{f,s\}} \chi(I_{4,i}) \frac{a_i}{2b_i} \left(e^{b_i(I_{4,i} - 1)^2} - 1 \right), \tag{58}$$

$$\psi_{vol} = \frac{\kappa}{2} (1 - J)^2, \tag{59}$$

$$\psi_{visc} = \frac{\eta}{2} \operatorname{tr}(\dot{\mathbf{E}}^2),\tag{60}$$

where a_i and b_i are material parameters, κ is a volumetric penalty parameter, and the strain invariants are defined as

$$ar{I}_1 = J^{-2/3}I_1$$
 , where $I_1 = \text{tr}(\mathbf{C})$, $I_{4,f} = \mathbf{f} \cdot \mathbf{C}\mathbf{f}$, $I_{4,s} = \mathbf{s} \cdot \mathbf{C}\mathbf{s}$, (61)

 $I_{8,fs} = \mathbf{f} \cdot \mathbf{C}\mathbf{s}$

 η is the viscosity and $\dot{\mathbf{E}}$ is the rate of Green–Lagrange strain tensor. $\chi(x)$ is a smoothed Heaviside function centered at x=1 with smoothing parameter k,

$$\chi(x) = \frac{1}{1 + \rho^{-k(x-1)}} \tag{62}$$

Finally, active stress is applied along fiber directions to recapitulate cardiac contraction,

$$\mathbf{S}_{act} = \tau(t) \cdot \mathbf{f} \otimes \mathbf{f}$$
. (63)

 $\tau(t)$ is determined using the model from [48], yielding the active stress curve shown in Fig. 6c (top).

On Γ_{epi} , we apply a Robin boundary condition in the normal direction only, following [48] to mimic the effect of the pericardium. On Γ_{base} , we apply Robin boundary conditions in all directions. On Γ_{endo} , we use a coupled Neumann boundary condition (Fig. 6a). The initial LV geometry is set as the stress-free reference configuration, and the simulation is initialized with zero displacements and velocities.

In this example, the 0D fluid is an open-loop Windkessel-type model of the systemic circulation [48], shown in Fig. 6a. Performing a nodal analysis on this LPN yields the following set of ODEs.

$$\frac{p_{v} - p_{at}}{R_{av}} + \frac{p_{v} - p_{p}}{R_{sl}} - Q_{1} = 0,$$

$$q_{p} - \frac{p_{v} - p_{p}}{R_{sl}} + C_{p}\dot{p}_{p} = 0,$$

$$q_{p} + \frac{p_{d} - p_{p}}{R_{p}} + \frac{L_{p}}{R_{p}}\dot{q}_{p} = 0,$$

$$\frac{p_{d} - p_{ref}}{R_{d}} - q_{p} + C_{d}\dot{p}_{d} = 0.$$
(64)

The atrial pressure p_{at} is a prescribed function of time, given by

$$p_{at} = \begin{cases} \frac{\Delta p_{at}}{2} \left(1 - \cos \frac{2\pi (t - t_{sys,a})}{T_{sys,a}} \right) + p_{at0}, & \text{for } t_{sys,a} < t < t_{sys,a} + T_{sys,a}, \\ p_{at0}, & \text{otherwise.} \end{cases}$$
(65)

See Fig. 6c (bottom) for plot.

The atrioventricular (av) and semilunar (sl) valves are modeled as diodes with nonlinear resistances R_{av} and R_{sl} that depend on the pressure differential on either side as below:

$$R_{av} = R_{min} + (R_{max} - R_{min})S^{+}(p_v - p_{at}),$$
(66)

$$R_{sl} = R_{min} + (R_{max} - R_{min})S^{+}(p_n - p_n),$$
 (67)

where S^+ is a sigmoid function with steepness parameter k_p .

To cast into the general form in Section 2.3, we identify the 0D unknowns as $\mathbf{w} = [p_v, p_p, p_d, q_p]^T$, while the coupled Dirichlet boundary data are $\mathbf{Q} = [Q_1]^T$. The uncoupled Neumann boundary data are $\mathbf{p} = [p_{al}, p_{ref}]^T$, and there are no uncoupled Dirichlet boundary data $\mathbf{q}_u = []$. The 0D variables are initialized using values from [48]. The coupled problem for this example can be summarized as

$$\begin{cases} \mathcal{P}^{0D}(\mathbf{w},t,[\mathbf{q}_{u},\mathbf{Q}],\mathbf{p})=\mathbf{0} & \text{given by Eq. (64),} \\ \text{Initial conditions from [48],} \\ \\ \mathcal{P}^{3D,struct}(\mathbf{u},\mathbf{x},t)=\mathbf{0}, \\ \text{Initialize with zero displacement and velocity,} \\ \text{(Uncoupled) Robin boundary conditions on } \Gamma_{epi} \text{ and } \Gamma_{base}, \\ \\ \sigma \cdot \mathbf{n}=-P_{1}\mathbf{n}, \text{ on } \Gamma_{endo}, \\ \\ P_{1}(t)=w_{1}(t)=p_{v}(t), \\ Q_{1}(t)=\int_{\Gamma_{endo}(t)}\mathbf{u}(t) \cdot \mathbf{n}(t)d\Gamma. \end{cases} \tag{68}$$

A complete table of parameters for this simulation can be found in Appendix D Table 1.

Fig. 7 (left) shows the pressure–volume (PV) loop over 10 cardiac cycles obtained from this coupled simulation. Although the initial volume of the idealized LV is higher than a physiological heart, the ranges of pressure and volume are in a physiological range. The stroke volume is approximately 90 mL and the resulting ejection fraction is 50%, which is comparable to normal physiological values and values reported in other computational studies with different LV geometries [22,48,50]. There is a clear delineation of

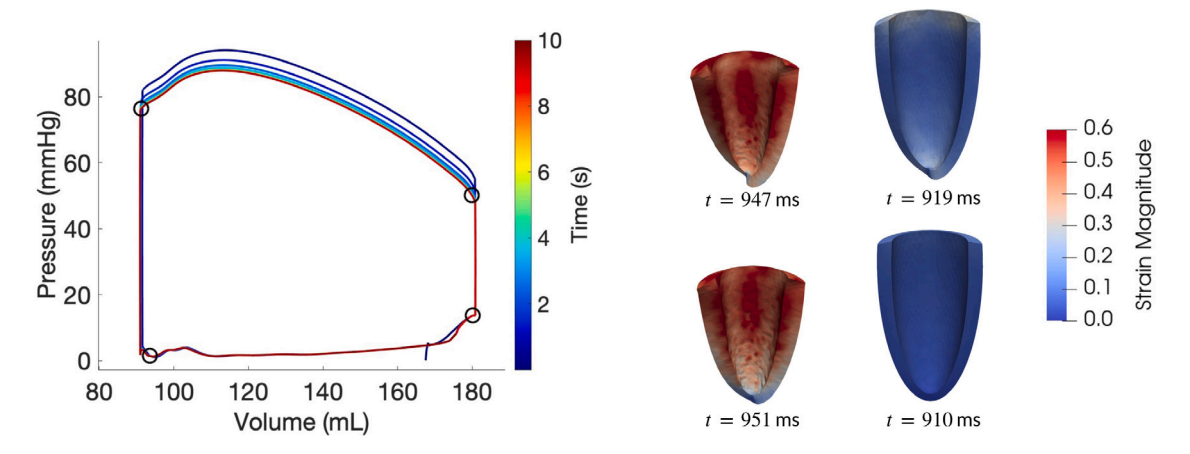


Fig. 7. Left: The PV loop for the LV is plotted for 10 cardiac cycles. The PV loop spans a realistic range of pressure and volume, exhibits a clear distinction of the four cardiac phases, and reaches a limit cycle after about 5 cardiac cycles. Right: The deformation of the LV, colored by the magnitude of Green-Lagrange strain, is shown at four time points in the final (tenth) cardiac cycle, corresponding to the black circles on the PV loop. A movie showing the LV deformation synchronized with the PV loop is provided in the supplementary material. (For interpretation of the references to color in this figure legend, the reader is referred to the web version of this article.)

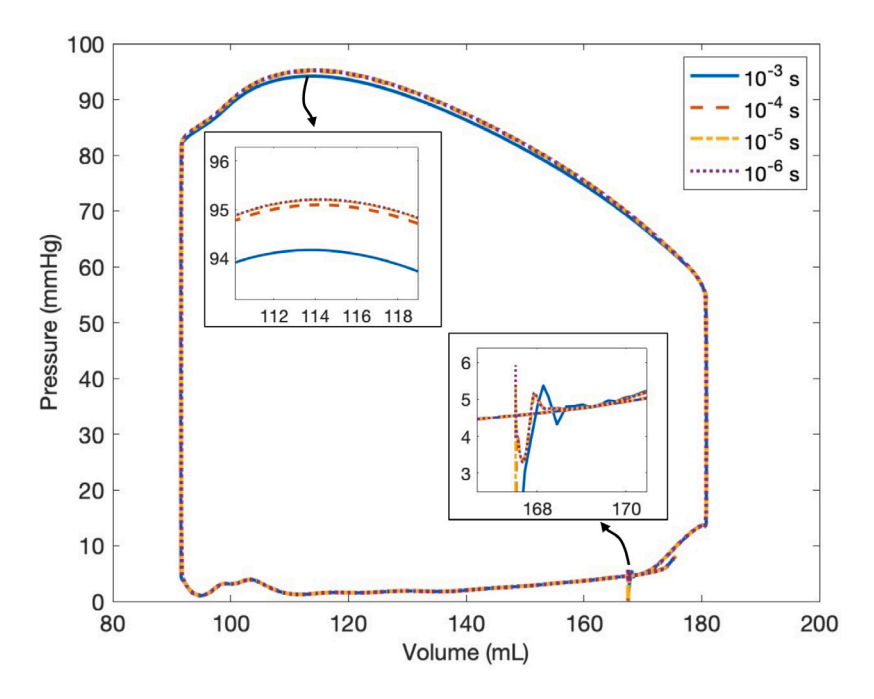


Fig. 8. PV loops for a single cardiac cycle of the idealized LV model (Section 3.1) for decreasing timestep size. Insets show zoomed in view at the top and bottom-right portions of the loop. PV loops converge as the timestep size decreases.

the four cardiac phases — isovolumic contraction, ejection, isovolumic relaxation, and filling. Additionally, the PV loop reaches a limit cycle after about 5 cardiac cycles.

Fig. 7 (right) shows the LV deformation, colored by the magnitude of Green–Lagrange strain, $\|\mathbf{E}\|_F$, at four time points in the final (tenth) cardiac cycle. These time points correspond to the black circles shown in Fig. 7 (left), at the transition points between cardiac phases when the cardiac valves open or close. Just before isovolumic contraction ($t = 910 \,\mathrm{ms}$), the LV is at its maximum volume and relatively unstrained, being loaded only by an end-diastolic pressure of 13.5 mmHg. After isovolumic contraction ($t = 919 \,\mathrm{ms}$), LV volume is nearly unchanged, but the LV has begun to exhibit its characteristic twist due the prescribed fiber architecture, seen most clearly by the rotation of the apex. Just before isovolumic relaxation ($t = 947 \,\mathrm{ms}$), when the fiber stress is maximum and the LV is the most deformed and at its minimum volume, strain magnitude is greatest. Finally, after isovolumic relaxation ($t = 951 \,\mathrm{ms}$), LV volume is still at its minimum value, but the LV has begun to untwist due to the relaxation of the fiber stress.

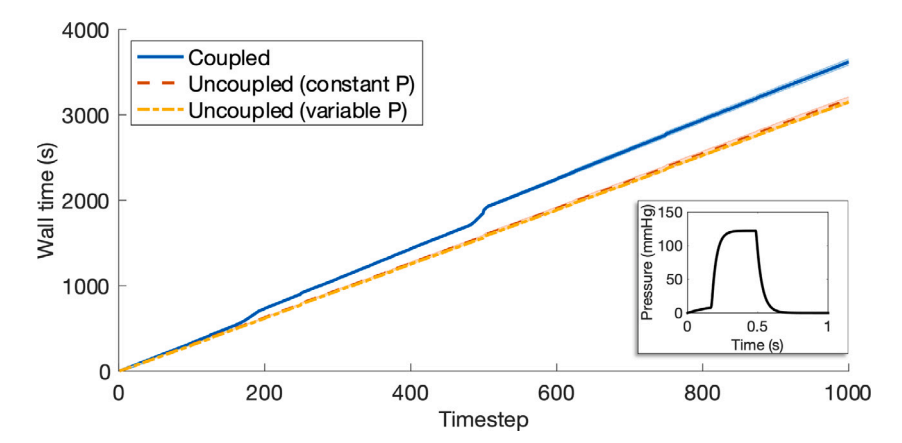


Fig. 9. Comparison of simulation time for 0D-coupled versus uncoupled simulations. "Coupled" is identical to that in Fig. 6, except it is run for only 1 cardiac cycle (1000 timesteps). "Uncoupled (constant P)" is the same except the endocardial pressure is a constant 1500 Pa (11.25 mmHg). "Uncoupled (variable P)" is the same except the endocardial pressure is given by a prescribed time-varying pressure curve, shown in the inset plot. All simulations were run in parallel with 4 processors. Each simulation was run 5 times, and the mean \pm standard deviation of those samples is plotted.

3.2. Temporal convergence

In this section, we present preliminary results on the temporal convergence of the coupling method, applied to the idealized LV model (Section 3.1). In Fig. 8, the PV loop for a single cardiac cycle of the LV model is plotted for several timestep sizes. As the timestep size is decreased from 10^{-3} s to 10^{-6} s, the PV loop converges. As shown in the figure, the PV loop for 10^{-3} s is very close to the PV loop for 10^{-6} s, except for the maximum pressure, for which the difference is only about 1%.

3.3. Computational cost

In this section, wall time is used to compare the computational cost of the 0D-coupled idealized LV simulation (Section 3.1) with two similar but uncoupled simulations — the first with a constant endocardial pressure, and the second with a time-varying endocardial pressure. All simulations were run for one cardiac cycle (1000 timesteps) with a timestep size of 10^{-3} s. All simulations were run in parallel with 4 CPUs of an Intel Gold 5118 2.3 GHz processor, and each case was run 5 times. The mean wall time \pm standard deviation was computed for each set of simulations. As seen in Fig. 9, after one cardiac cycle, the coupled simulation is approximately 15% slower than the uncoupled simulations. This is due to the extra 0D solver communication and computation that is performed at each Newton iteration of the 3D solver. Note also that around timesteps 200 and 500, the coupled simulation slows down. These timesteps correspond to the isovolumic phases when both valves are closed, where our method experiences marginally slower convergence.

3.4. Inflation of a spherical shell through its limit point

An interesting feature of the coupling framework is that it also permits the investigation of so-called limit point problems in structural mechanics. In this example, a simple 0D LPN is used to inflate a thick-walled sphere at approximately a constant flowrate (Fig. 10). The coupled problem for this example may be stated in the structure of Eq. (34) as

$$\begin{cases} p_{in} = p_{high} + Q_1 R_{high}, \\ \mathcal{P}^{3D,struct}(\mathbf{u}, \mathbf{x}, t) = \mathbf{0}, \\ \text{Initialize with zero displacement and velocity,} \\ \sigma \cdot \mathbf{n} = -P_1 \mathbf{n}, \text{ on } \Gamma_{inner}, \\ P_1(t) = w_1(t) = p_{in}(t), \\ Q_1(t) = \int_{\Gamma_{inner}(t)} \mathbf{u}(t) \cdot \mathbf{n}(t) d\Gamma. \end{cases}$$

$$(69)$$

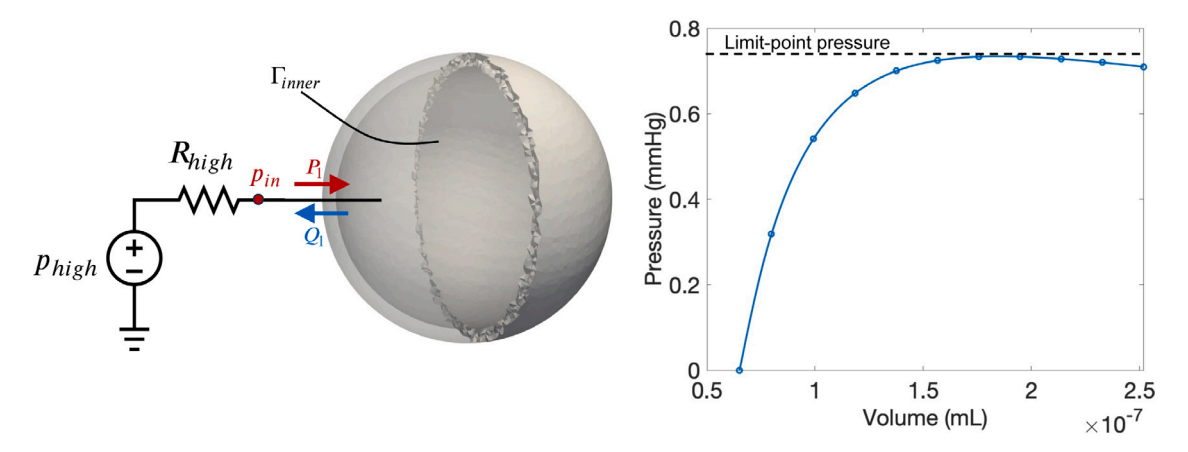


Fig. 10. Left: A 3D thick spherical shell is coupled to a constant current 0D fluid. The inner surface of the shell is the coupled Neumann boundary. The 0D fluid model has a high pressure source and a high resistance, which produces an approximately constant flowrate. Right: The pressure–volume relation for the spherical shell is plotted. Markers are placed every 100 ms. Inflating the sphere at roughly a constant rate of change of volume allows the limit point (where dP/dV = 0) to be traversed.

The LPN is the simplest "constant current" circuit, consisting of a large resistance R_{high} and a large pressure source p_{high} , chosen together to yield an approximately constant flowrate $-Q_1$ into the sphere. In this case, the LPN is described by a single algebraic equation for the pressure inside the sphere, $\mathbf{w} = [p_{in}]^T$. The coupled 0D Dirichlet boundary data are $\mathbf{Q} = [Q_1]^T$. The uncoupled 0D Neumann boundary data are $\mathbf{p} = [p_{high}]^T$, and there are no uncoupled 0D Dirichlet boundary data $\mathbf{q}_u = []$. By the coupling conditions, the pressure P_1 applied to the inner surface of the sphere, Γ_{inner} , is equal to p_{in} .

The sphere has an inner radius of $25 \, \mu m$ and a thickness of $2.5 \, \mu m$, and it is composed of a neo-Hookean material with material constant $C_1 = 3 \, k Pa$. The geometry is meshed with linear tetrahedral elements with an average edge length of approximately $1 \, \mu m$, yielding a mesh with 229,578 elements and 42,673 nodes (128,019 degrees of freedom). With the given geometry and material model, the spherical shell displays limit point behavior. Specifically, as the sphere is inflated in a quasi-static process, the pressure increases, reaches a maximum (the limit point, where dP/dV=0), then decreases [51,52] (Fig. 10 right). Similar concave down diastolic pressure–volume relations have been observed in embryonic chick hearts [53] and embryonic zebrafish hearts [54], and limit point behavior has been proposed as a possible explanation. This example represents an idealized model of this phenomena in small-scale, embryonic hearts.

Limit point behavior presents a challenge to standard simulation methods. To simulate inflation of the sphere, one would typically apply an increasing pressure on the inner surface at constant increments. Unfortunately, this approach would never be able to capture the descending portion of the PV curve; once the applied pressure exceeds the limit point pressure, Newton's method will diverge and the simulation will crash because there is no static equilibrium configuration at that pressure. Techniques exist to traverse the limit point (and similar phenomena like snap-through behavior), the most common being the arc-length method [55].

As shown in Fig. 10, the present coupling framework allows us to traverse this limit point. There is in fact a connection between this coupling method and the arc-length method. In both cases, the load magnitude (pressure) is treated as unknown, and the equations corresponding to the mechanics problem are augmented by additional equations required to determine the load increment or load scaling factor. Actually, ANM was originally applied to solve coupled nonlinear systems arising from the arc-length method [34]. We note that a standard monolithic 3D–0D coupling approach, such as in [20], should also be able to traverse limit points in the same manner, but to the best of our knowledge, no previous studies have applied it to limit point problems.

3.5. 3D fluid - 0D fluid example

For completeness, and to illustrate the generality of the coupling scheme to both 3D structure–0D fluid problems and 3D fluid–0D fluid problems, we reproduce a simulation similar to those in [56] using the current coupling scheme. In this work, the authors applied the original 3D fluid–0D fluid coupling of [19] to simulate blood flow in the pulmonary arteries coupled to a complex, closed-loop model of the cardiovascular system. They used this model to investigate the hemodynamic effects of left pulmonary artery stenosis after the stage II superior cavo-pulmonary connection (SCPC) surgery. The model is illustrated in Fig. 11. The geometry is meshed with linear tetrahedral elements with an average edge length of approximately 0.3 mm yielding a mesh with 1,593,709 elements and 293,943 nodes (881,829 degrees of freedom). The parameters of the model are taken from Table E1 P2 in [56].

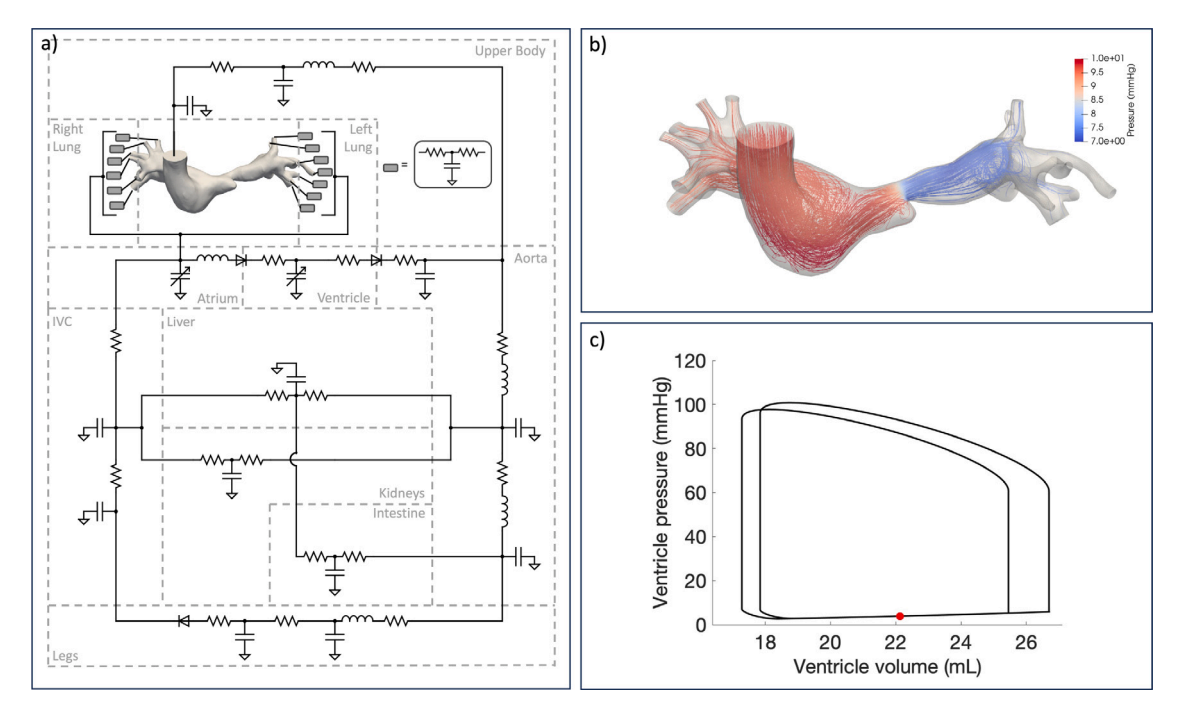


Fig. 11. (a) A 3D model of the pulmonary arteries is coupled to a closed-loop LPN model of the circulatory system [56]. (b) Streamlines of blood flow, colored by pressure, in the pulmonary arterial model during mid-diastole (see red dot in the PV loop in panel c). (c) The PV loop over two cardiac cycles of the LPN ventricle, which is modeled as a time-varying capacitor. (For interpretation of the references to color in this figure legend, the reader is referred to the web version of this article.)

The coupled problem for this example may be stated as,

```
\begin{cases} \mathcal{P}^{0D}(\mathbf{w},t,[\mathbf{q}_{n},\mathbf{Q}],\mathbf{p})=\mathbf{0} \text{ (equations not provided),} \\ \text{Initial conditions,} \\ \mathcal{P}^{3D,fluid}(\mathbf{u},p,\mathbf{x},t)=\mathbf{0}, \\ \text{Initial conditions,} \\ \text{(Uncoupled) no-slip boundary conditions on walls,} \\ \boldsymbol{\sigma}\cdot\mathbf{n}=-P_{1}\mathbf{n}, \text{ on } \Gamma_{h_{c}}^{(1)}, \\ \vdots \\ \boldsymbol{\sigma}\cdot\mathbf{n}=-P_{14}\mathbf{n}, \text{ on } \Gamma_{h_{c}}^{(14)}, \\ \vdots \\ P_{1}(t)=(\mathbb{P}\mathbf{w}(t))_{1}, \\ \vdots \\ P_{14}(t)=(\mathbb{P}\mathbf{w}(t))_{14}, \\ Q_{1}(t)=\int_{\Gamma_{h_{c}}^{(14)}(t)}\mathbf{u}(t)\cdot\mathbf{n}(t)d\Gamma, \\ \vdots \\ Q_{14}(t)=\int_{\Gamma_{h_{c}}^{(14)}(t)}\mathbf{u}(t)\cdot\mathbf{n}(t)d\Gamma, \end{cases}
```

where $\Gamma_{h_c}^{(1)}, \dots, \Gamma_{h_c}^{(14)}$ are the 14 faces (1 inlet + 13 outlet) of the pulmonary model, which are associated with 14 coupling pressures $P_1 \dots P_{14}$ and flowrates $Q_1 \dots Q_{14}$.

For the sake of clarity, when applied to 3D fluid–0D fluid problems, the coupling code used in the present work is functionally identical to the code used in [56]. We include this section to emphasize that a 3D fluid–0D fluid problem can be solved using the current unified coupling scheme; however, the method when applied to the 3D fluid–0D fluid problem and the results in this section are not novel.

Fig. 11 shows the 3D fluid and 0D fluid models, as well as the simulation results, which include a visualization of blood flow in the pulmonary arteries and the PV loop of the LPN ventricle component. Other examples of 3D fluid-0D fluid coupling using the present coupling method can be found in [19,57,58].

4. Discussion

We present a general framework for coupling 3D models of cardiovascular components – cardiac structures like the LV, as well as vascular blood flow models like the pulmonary arteries – to 0D models of the circulatory system. The novel aspects of this work are the extension of the modular framework of [19] to the 3D structure–0D fluid problem, a demonstration of the scheme's efficacy in 0D-coupled cardiac mechanics applications, especially in its ability to avoid the balloon dilemma and capture isovolumic cardiac phases, and finally a new derivation of the coupling scheme based on ANM, which provides important mathematical underpinnings and clearly shows the close connection to the monolithic coupling approach.

In multiple examples, we have shown the effectiveness of the present coupling method. To illustrate the application to cardiac mechanics modeling, we simulated an idealized LV coupled to an open-loop LPN over 10 cardiac cycles (Section 3.1). The resulting PV loop spans physiological ranges of pressure and volume, shows a clear distinction of the four cardiac phases, and reaches a limit cycle. Critically, the isovolumic phases of the cardiac cycle are automatically captured without numerical stability issues. These results provide significant verification of the effectiveness of the coupling framework for cardiac mechanics simulations. Using the coupled LV model, we made preliminary assessments of the temporal convergence and cost of our method. In Section 3.2, we showed that the coupling algorithm is stable and converges for small timesteps. In Section 3.3, we showed that coupled simulations are moderately more expensive than uncoupled simulations (15% longer for one cardiac cycle). The additional cost comes from communication with the 0D solver and a few assembly operations each Newton iteration of the 3D solver. This relatively small increase in cost is well-warranted, given the increased physiological fidelity afforded by the coupling. In the spherical shell inflation case (Section 3.4), which represents a simplified model of an embryonic heart, we showed 3D–0D coupling can be used to traverse a limit point and discussed its relationship to the arc-length method. Finally, we simulated blood flow in a pulmonary arterial model coupled to a closed-loop LPN of the circulatory system, demonstrating that our coupling also applies to the 3D fluid–0D fluid problem (Section 3.5).

Previous approaches to the coupling problem use either a partitioned or monolithic strategy, and the advantage of the present coupling is that it adopts a hybrid strategy, retaining the attractive features of both. In a monolithic approach, such as [20,48], modifying the 0D model can be cumbersome, requiring a detailed understanding of the 3D solver structure. In particular, one must typically derive new expressions for the off-diagonal tangent blocks in the monolithic (Newton) linear system Eq. (36). In our approach, one can modify the 0D model without touching the 3D solver at all, and vice versa. As shown in Section 2, this is achieved by applying Schur complement reduction to Eq. (36), which separates the 3D and 0D computations, then using the 0D fixed point operator to approximately solve the modified linear system.

The present approach corresponds to the Neumann coupling in [19], in which a Neumann (pressure) boundary condition is imposed on the 3D domain, while a Dirichlet boundary condition is imposed on the 0D domain. In [19], the authors also described a Dirichlet coupling, in which a Dirichlet boundary condition is imposed on the 3D domain, while a Neumann boundary condition is imposed on the 0D domain. In this type of coupling, the shape of the velocity profile on the 3D Dirichlet surface must be chosen. While applicable to fluid simulations, in which one can reasonably assume a parabolic or flat profile, this is an inconvenient limitation for structural mechanics simulations, since in most cases, the shape of the velocity profile cannot reasonably be assumed a priori. In this paper, we only consider Neumann coupling.

A different kind of Dirichlet coupling for the 3D structure–0D fluid problem may be achieved by imposing a volume for the 3D structure, enforced by augmenting the structural equations with a volume constraint, as in recent works [21,22,29]. The augmented equations are then solved using Newton-like methods. Our Neumann coupling approach does not require such a volume constraint. Furthermore, unlike in the time-staggered approach of [29], we do not observe any unphysical oscillations in the LV test case. These oscillations, which were mitigated by the addition of a stabilization term in [29], do not appear in our coupling approach because we iterate until both 3D and 0D systems are converged at each timestep. Similar oscillations might appear between iterations within a timestep, but these are mitigated in our scheme by the incorporation of resistance information into the 3D tangent matrix, which in fact is similar in philosophy to the stabilization term in [29].

The authors of [19] also identified three variations of the method. In the "implicit" method, the M matrix is updated each Newton iteration. In the "semi-implicit" method, M is only computed once at the start of the simulation. In the "explicit" method, the entire 0D contribution to the 3D tangent matrix is ignored. Note that this variation is nearly identical to the nonlinear Gauss–Seidel approach mentioned in Section 2.4, except instead of solving the 3D residual equation fully each coupling iteration, the 3D solver takes only one Newton step each coupling iteration. In [19], the three variations were compared in 3D fluid–0D fluid test cases, and the semi-implicit method was found to provide the best balance of stability and cost. In this work, we described and used only the implicit method because, for the coupled LV simulation, the explicit method was unstable due to the balloon dilemma, and the semi-implicit method did not converge because M changes drastically over the simulation due to the opening and closing of the cardiac valves. We leave a detailed comparison of the three variations for coupled cardiac mechanics simulations to future work.

Limitations and future work With respect to the present coupling algorithm, we identify important areas for future investigation and development. We will first analyze the temporal convergence of the method, including the order of convergence as well as the effect of the 3D and 0D time-stepping schemes on overall convergence. In addition, under certain assumptions met in our case, ANM should converge quadratically [34]. We intend to verify this quantitatively.

We are also interested in applying the stabilized structural mechanics formulation presented in [59] for cardiac mechanics simulations. This formulation treats both fluid and structural problems under a unified continuum modeling framework in which pressure is a primitive variable. It is highly effective for incompressible solids, including cardiac tissues. Generally, we plan on applying the coupling in more complex cardiac mechanics simulations, for example with advanced myocardial constitutive models [27,60] or using 4-chamber anatomies [26].

This framework can be extended to couple a 3D model to a 1D model of blood circulation [61], which, unlike a 0D model, can recapitulate wave propagation phenomenon in arteries [62]. On the 3D side, the expressions will be identical. One only needs to define the effect of a flowrate boundary condition on the 1D system, and define how to extract pressure from the 1D system to communicate back to the 3D system.

In the coupled LV test case, we assumed all cardiac muscle fibers contract in unison. While this assumption was sufficient to generate many key features of cardiac behavior, in reality, the propagation of an electrical excitation wave determines the timing of contraction at various points in the heart muscle. In future work, we plan on simulating the electrophysiology of the heart in order to recapitulate this mechanical dyssynchrony, which can be important in diseased cases like ventricular tachycardia or bundle branch blocks [63–65]. Coupling electrophysiology and 3D structural mechanics, with either one-way or two-way coupling approaches, is a challenging problem in its own right [22], but since electrophysiology is not directly coupled to the 0D fluid model, it can be integrated into the present 3D structure–0D fluid coupling framework with little or no modification.

Another important limitation in the coupled LV test case is the assumption of a spatially uniform endocardial pressure distribution, a consequence of using a 0D fluid model. Indeed, the blood pressure in the LV is not spatially homogeneous. Experimental studies have quantified the pressure difference between the apical and basal regions of the LV, called left ventricular pressure gradient (LVPG) or intraventricular pressure difference (IVPD). This value varies throughout the cardiac cycle, but for healthy adult humans, it is around 3 mmHg during diastole and a similar order of magnitude in systole [66–68]. However, this degree of spatial variability is much smaller than the temporal variability in LV pressure, which is roughly 100 mmHg. Thus, we argue that the spatially uniform pressure assumption is adequate to capture the major features of LV function. That said, spatial variability may be important to capture some phenomena, especially in diseased cases. In future work, we intend to evaluate the importance of spatial variability in LV pressure by comparing 0D-coupled LV simulations to FSI simulations with fully-resolved intraventricular blood flow.

Finally, more recent coupling ideas similar to ANM have been proposed and summarized in [69], in which each solver is treated as a blackbox defined only through its fixed point iteration operator. These algorithms are even more modular than the present coupling scheme, while retaining the quadratic convergence properties of Newton's method. Future work may aim to apply these ideas to the 3D–0D coupling discussed here.

5. Conclusion

In this work, a unified and modular framework for 3D–0D coupling in cardiovascular simulations is introduced. The algorithm, originally described in [19] for the 3D fluid–0D fluid problem, is extended to solve the closely-related 3D structure–0D fluid problem, showing that both problems can be treated uniformly within the same mathematical formulation. Through multiple examples, the effectiveness of the coupling algorithm is demonstrated. Notably, we construct a 0D-coupled idealized LV model that produces a physiological pressure–volume loop and effectively captures the isovolumic cardiac phases without additional numerical treatment. We also provide a new derivation using ANM, which reveals the present coupling scheme's connection to the monolithic Newton coupling approach. This hybrid coupling strategy combines the stability of monolithic approaches with the modularity and flexibility of partitioned approaches, with relatively small additional computational cost compared to uncoupled simulations. Overall, this work provides a robust, flexible, and efficient method for modeling the circulatory system in cardiovascular simulations of tissue mechanics and blood flow.

CRediT authorship contribution statement

Aaron L. Brown: Conceptualization, Data curation, Formal analysis, Investigation, Methodology, Software, Visualization, Writing – original draft. Matteo Salvador: Formal analysis, Supervision, Writing – review & editing. Lei Shi: Investigation, Methodology, Software. Martin R. Pfaller: Formal analysis, Methodology, Software, Writing – review & editing. Zinan Hu: Methodology, Software. Kaitlin E. Harold: Methodology, Software. Tzung Hsiai: Funding acquisition, Project administration. Vijay Vedula: Formal analysis, Investigation, Methodology, Software, Supervision, Writing – review & editing. Alison L. Marsden: Funding acquisition, Project administration, Supervision, Writing – review & editing.

Declaration of competing interest

The authors declare that they have no known competing financial interests or personal relationships that could have appeared to influence the work reported in this paper.

Data availability

Data will be made available on request.

Acknowledgments

Funding for this research was provided by the National Institutes of Health grants 5R01HL159970-02, 5R01HL129727-06, and K99HL161313. The authors wish to thank Dr. Erica Schwarz, Dr. Fannie Gerosa, and Reed Brown for their helpful discussions during this project and for their comments on this paper.

Appendix A. 4th order Runge-Kutta scheme

RK4 applied to the ODE system Eq. (25) reads

$$\mathbf{k}_{1} = \mathbf{f}\left(\mathbf{y}_{n}, \mathbf{z}_{n}, t_{n}, \mathbf{q}(t_{n}), \mathbf{p}(t_{n})\right),$$

$$\mathbf{k}_{2} = \mathbf{f}\left(\mathbf{y}_{n} + \mathbf{k}_{1} \frac{\Delta t}{3}, \mathbf{z}_{n}, t_{n} + \frac{\Delta t}{3}, \mathbf{q}(t_{n} + \frac{\Delta t}{3}), \mathbf{p}(t_{n} + \frac{\Delta t}{3})\right),$$

$$\mathbf{k}_{3} = \mathbf{f}\left(\mathbf{y}_{n} - \mathbf{k}_{1} \frac{\Delta t}{3} + \mathbf{k}_{2} \Delta t, \mathbf{z}_{n}, t_{n} + \frac{2\Delta t}{3}, \mathbf{q}(t_{n} + \frac{2\Delta t}{3}), \mathbf{p}(t_{n} + \frac{2\Delta t}{3})\right),$$

$$\mathbf{k}_{4} = \mathbf{f}\left(\mathbf{y}_{n} + \mathbf{k}_{1} \Delta t - \mathbf{k}_{2} \Delta t + \mathbf{k}_{3} \Delta t, \mathbf{z}_{n}, t_{n} + \Delta t, \mathbf{q}(t_{n} + \Delta t), \mathbf{p}(t_{n} + \Delta t)\right),$$

$$\mathbf{y}_{n+1} = \mathbf{y}_{n} + \frac{\mathbf{k}_{1} + 3\mathbf{k}_{2} + 3\mathbf{k}_{3} + \mathbf{k}_{4}}{8} \Delta t.$$

$$(71)$$

The algebraic variables are then determined by solving Eq. (26) for \mathbf{z}_{n+1} with the updated differential variables \mathbf{y}_{n+1} ,

$$\mathbf{g}(\mathbf{y}_{n+1}, \mathbf{z}_{n+1}, t_n + \Delta t, \mathbf{q}(t_n + \Delta t), \mathbf{p}(t_n + \Delta t)) = \mathbf{0}.$$

For the LPNs considered in this work, this equation can be rewritten as

$$\mathbf{z}_{n+1} = \tilde{\mathbf{g}}(\mathbf{y}_{n+1}, \mathbf{z}_{n+1}, t_n + \Delta t, \mathbf{q}(t_n + \Delta t), \mathbf{p}(t_n + \Delta t)),$$

for some function $\tilde{\mathbf{g}}$. If the LPN contains valves (as in the LV example in Section 3.1), $\tilde{\mathbf{g}}$ is highly nonlinear with respect to \mathbf{z}_{n+1} . This leads to numerical difficulties in the coupling associated with valves switching open and closed between subsequent Newton iterations. These difficulties are alleviated by replacing \mathbf{z}_{n+1} with \mathbf{z}_n ,

$$\mathbf{z}_{n+1} = \tilde{\mathbf{g}}(\mathbf{y}_{n+1}, \mathbf{z}_n, t_n + \Delta t, \mathbf{q}(t_n + \Delta t), \mathbf{p}(t_n + \Delta t)). \tag{72}$$

Note that we assume the flow and pressure boundary forcings, \mathbf{q} and \mathbf{p} , are known functions of time. In the coupled problem, \mathbf{q} is composed of a prescribed uncoupled component \mathbf{q}_u and a coupled component \mathbf{Q} ,

$$\mathbf{q}(t) = [\mathbf{q}_u(t), \mathbf{Q}(t)].$$

Since \mathbf{q}_u is prescribed, its value is known at any time t. The value of \mathbf{Q} , on the other hand, is obtained from the 3D system, and its variation with time may be approximated by interpolating between its values at timestep n and n+1,

$$\mathbf{Q}(t_n + h) = \mathbf{Q}_n + (\mathbf{Q}_{n+1} - \mathbf{Q}_n) \frac{h}{\Lambda t},$$

where \mathbf{Q}_n and \mathbf{Q}_{n+1} are calculated from the 3D degrees of freedom Φ_n and Φ_{n+1} , respectively.

From Eqs. (71) and (72), we can identify the fixed point operator corresponding to this 0D time integration scheme as

$$\begin{split} F^{0D,RK4}(\mathbf{w}_{n+1}, \boldsymbol{\Phi}_{n+1}; \mathbf{w}_n, \boldsymbol{\Phi}_n) &= \begin{bmatrix} \mathbf{y}_{n+1} \\ \mathbf{z}_{n+1} \end{bmatrix} \\ &= \begin{bmatrix} \mathbf{w}_n + \frac{\mathbf{k}_1 + 3\mathbf{k}_2 + 3\mathbf{k}_3 + \mathbf{k}_4}{8} \Delta t \\ \tilde{\mathbf{g}} \Big(\mathbf{w}_n + \frac{\mathbf{k}_1 + 3\mathbf{k}_2 + 3\mathbf{k}_3 + \mathbf{k}_4}{8} \Delta t, \mathbf{z}_n, t_n + \Delta t, \mathbf{q}(t_n + \Delta t), \mathbf{p}(t_n + \Delta t) \Big) \end{bmatrix}. \end{split}$$

Appendix B. Calculation of flowrate

For a coupled Neumann boundary condition, the 3D model must compute a flowrate Q and send this value to the 0D domain. For 3D fluid–0D fluid coupling (e.g., blood flow in the aorta coupled to Windkessel LPN), this is easily computed by integrating the normal component of the velocity over the coupled surface, $Q = \int_{\Gamma} \mathbf{u} \cdot \mathbf{n} d\Gamma$. For structural simulations, we must specify the context. In cardiac mechanics, we are typically interested in modeling a chamber or chambers of the heart. In this context, we are interested in the flowrate of blood into or out of a chamber, which is identical to the rate of change of volume of the chamber. We use this interpretation to compute flowrate in the 3D structure–0D fluid problem.

Let Γ be a closed surface, for example a sphere. The rate of change of volume enclosed by Γ can be computed using the Reynolds Transport Theorem, which states that for an arbitrary scalar function f defined over a time-varying region $\Omega(t)$ with boundary $\Gamma(t)$

$$\frac{d}{dt} \int_{\Omega(t)} f d\Omega = \int_{\Omega(t)} \frac{\partial f}{\partial t} d\Omega + \int_{\Gamma(t)} (\mathbf{u_b} \cdot \tilde{\mathbf{n}}) f d\Gamma, \tag{73}$$

where $\mathbf{u_b}$ is the velocity of the boundary and $\tilde{\mathbf{n}}$ is the outward unit normal of the boundary. Taking f=1 and observing that $\frac{\partial f}{\partial t}=0$, we find

$$\frac{d}{dt} \int_{\Omega(t)} (1) d\Omega = \int_{\Omega(t)} 0 d\Omega + \int_{\Gamma(t)} (\mathbf{u_b} \cdot \tilde{\mathbf{n}}) (1) d\Gamma,$$

$$\frac{dV}{dt} = \int_{\Gamma(t)} (\mathbf{u_b} \cdot \tilde{\mathbf{n}}) d\Gamma. \tag{74}$$

That is, the rate of change of volume enclosed by a surface Γ is the velocity flux integral over that surface. In cardiac mechanics, it is more natural to use the inward surface normal $\mathbf{n} = -\tilde{\mathbf{n}}$ (pointing away from the cardiac tissue and into the blood pool on the endocardial surface, for example). In addition, a positive flowrate Q out of the heart chamber is associated with a decrease in chamber volume. Thus, we may write

$$Q = -\frac{dV}{dt} = \int_{\Gamma(t)} (\mathbf{u_b} \cdot \mathbf{n}) d\Gamma. \tag{75}$$

This is in fact the same integral as in blood flow simulations, except we must be careful to take the integral over the coupled surface in the current (deformed) configuration, $\Gamma(t)$.

It is important to note that Eq. (75) is valid only if Γ is a closed surface. In general, this is not the case, for example in the left ventricle or biventricle models cut at the basal plane. For these models, in order to accurately calculate $\frac{dV}{dr}$, it is necessary to close Γ with a "cap" surface. Such a capping was done in this work and slightly modifies the expressions for the 0D residual and tangent contributions (see Section 2.6).

Appendix C. Contribution of coupled surface to tangent matrix

Here we derive Eq. (55) from Eq. (53). Eq. (53) reads

$$\left[\mathbf{K}^{3D/0D}\right]_{n+1}^{(k)} = \left[\frac{\partial \mathbf{R}^{3D}}{\partial \mathbf{P}_{n+1}} \mathbb{P} \frac{\partial F^{0D}(\mathbf{w}_{n+1}, \mathbf{Q}_{n+1})}{\partial \mathbf{Q}_{n+1}} \frac{\partial \mathbf{Q}_{n+1}}{\partial \mathbf{U}_{n+1}} \frac{\partial \mathbf{U}_{n+1}}{\partial \mathbf{\Phi}_{n+1}}\right]_{n+1}^{(k)}.$$

We consider each term individually.

• The residual \mathbf{R}^{3D} depends on the coupling pressures \mathbf{P}_{n+1} through an equation like Eq. (49),

$$R_{Ai}^{3D} = \text{other terms} + \sum_{j=1}^{n^{cBC}} \int_{\Gamma_{h_c}^{(j)}} N_A P_{n+1,j} n_i d\Gamma.$$

Thus,

$$\frac{\partial(R_{Ai}^{3D})}{\partial P_{n+1,j}} = \int_{\Gamma_{h_{n}}^{(j)}} N_{A} n_{i} d\Gamma. \tag{76}$$

Note that if the 3D residual is composed of momentum and continuity components (e.g., for Navier–Stokes), then this term is multiplied by $\mathbb{I}_m = \begin{bmatrix} 1 \\ 0 \end{bmatrix}$, which is simply a vector with 1s corresponding to momentum rows and 0s corresponding to continuity rows. This places the tangent contribution in the momentum block row.

- rows. This places the tangent contribution in the momentum block row.

 In Section 2.4.3, we described how $\mathbb{P} \frac{\partial F^{0D}(\mathbf{w}_{n+1}, \mathbf{Q}_{n+1})}{\partial \mathbf{Q}_{n+1}}$ is computed in a finite difference manner (Eq. (54)). This term is denoted by the resistance matrix M_{ij} .
- From Eq. (32), we have

$$Q_{n+1,i} = \sum_{A} \int_{\Gamma_{h_c}^{(i)}} N_A U_{n+1,Ak} n_k d\Gamma.$$

Thus,

$$\frac{\partial Q_{n+1,i}}{\partial U_{n+1,Ak}} = \int_{\Gamma_{h_c}^{(i)}} N_A n_k d\Gamma. \tag{77}$$

• Finally, we deal with the term $\frac{\partial \mathbf{U}_{n+1}}{\partial \Phi_{n+1}}$. This term depends on the time discretization scheme. In our case, we use the generalized- α method and choose the nodal accelerations $\dot{\mathbf{U}}$ as our 3D unknowns (along with nodal pressures Π if the 3D is a fluid). The nodal velocities \mathbf{U} are related to the nodal accelerations $\dot{\mathbf{U}}$ by Eq. (33)

$$\mathbf{U}_{n+1} = \mathbf{U}_n + \Delta t \dot{\mathbf{U}}_n + \gamma \Delta t (\dot{\mathbf{U}}_{n+1} - \dot{\mathbf{U}}_n).$$

Thus,

$$\frac{\partial U_{n+1,Ai}}{\partial \Phi_{n+1,Bj}} = \frac{\partial U_{n+1,Ai}}{\partial \dot{U}_{n+1,Bj}} = \gamma \Delta t \delta_{AB} \delta_{ij}. \tag{78}$$

Note that if the 3D degrees of freedom contain both acceleration and pressure components (e.g., for Navier–Stokes), then this term is multiplied by $\mathbb{I}_a = \begin{bmatrix} 1 \\ 0 \end{bmatrix}$, which is simply a vector with 1s corresponding to acceleration rows and 0s corresponding to pressure rows. This places the tangent contribution in the acceleration block column.

Combining these terms yields the tangent matrix contribution Eq. (55). In addition to this tangent matrix contribution, with a follower pressure load there should be a tangent contribution due to the fact that $\Gamma_{h_c}^{(i)}$ and n_i change with the deformation. However, this term is no different than the required term for an uncoupled surface and is unrelated to our coupling method, so we do not explain it here.

Appendix D. Idealized LV simulation parameters

We list the parameter values for the idealized LV coupled to open-loop LPN simulation, shown in Fig. 6. Most values are taken from [48].

Table of simulation parameters for the LV test case shown in Fig. 6.

Name	Parameter	Value	Unit
General mechanical			
Tissue Density	$ ho_0$	10^{3}	kg/m ³
Viscosity	η	10^{2}	Pa s
Volumetric Penalty	κ	10^{6}	Pa
Active stress [48]			
Contractility	σ_0	8×10^{4}	Pa
Activation rate	α_{max}	+5	1/s
Deactivation rate	α_{min}	-30	1/s
Ventricular systole	t _{svs.v}	0.143	S
Ventricular diastole	$t_{dias,v}$	0.484	S
Steepness	γ	0.005	S
Passive myocardial tissue (HO model)			
Matrix	a	59.0	Pa
	b	8.023	_
Fiber	a_f	18.472×10^{3}	Pa
	b_f	16.026	_
Sheet	a_s	2.481×10^{3}	Pa
	b_s	11.12	_
Fiber sheet	a_{fs}	216	Pa
	b_{fs}	11.436	_
Epicardial boundary condition			
Spring stiffness	k_{epi}	1.0×10^{8}	Pa/m
Dashpot viscosity	c_{epi}	5.0×10^{3}	Pa s/m
Basal boundary condition	*		
Spring stiffness	k_{base}	1.0×10^{5}	Pa/m
Dashpot viscosity	c_{base}	5.0×10^{3}	Pa s/m
LPN	buse		
Proximal inertance	L_p	1.3×10^{5}	kg/m ⁴
Proximal capacitance	C_p	7.7×10^{-9}	$m^4 s^2/kg$
Distal capacitance	C_d	8.7×10^{-9}	$m^4 s^2/kg$
Proximal resistance	R_p	7.3×10^6	kg/m ⁴ /s
Distal resistance	R_d	1.0×10^{8}	kg/m ⁴ /s
Reference pressure	P_{ref}	0.0	Pa
Closed valve resistance	R _{max}	1×10^9	kg/m ⁴ /s
Open valve resistance	R_{max} R_{min}	1×10^{6}	kg/m ⁴ /s
Valve steepness	k_p	1×10^{-3}	Pa
Baseline atrial pressure	$P_{at,0}$	6.0	mmHg
Pressure	Pat,0		
		(contin	ued on next page

(continued on next page)

Table 1 (continued).

Name	Parameter	Value	Unit
Atrial pressure amplitude	Δp_{at}	8.0	mmHg
Atrial systole	$t_{sys,a}$	0.0	S
	$T_{sys,a}$	0.2	S
LPN initial conditions			
Initial ventricle pressure	$p_{v}(0)$	8.0	mmHg
Initial proximal pressure	$p_p(0)$	61.8	mmHg
Initial distal pressure	$p_d(0)$	59.7	mmHg
Initial proximal flowrate	$q_p(0)$	38.3	mL/s
Numerical integration			
Timestep size	Δt	0.001	S
Gen- α parameter	γ	0.5	_
Gen-α parameter	α_f	0.5	_
Gen- α parameter	α_m	0.5	_
Gen-α parameter	β	0.25	_

Appendix E. Supplementary data

Supplementary material related to this article can be found online at https://doi.org/10.1016/j.cma.2024.116764.

References

- [1] Erica L Schwarz, Luca Pegolotti, Martin R Pfaller, Alison L Marsden, Beyond CFD: Emerging methodologies for predictive simulation in cardiovascular health and disease, Biophys. Rev. 4 (1) (2023) 011301.
- [2] Alison L Marsden, Adam J Bernstein, V Mohan Reddy, Shawn C Shadden, Ryan L Spilker, Frandics P Chan, Charles A Taylor, Jeffrey A Feinstein, Evaluation of a novel Y-shaped extracardiac fontan baffle using computational fluid dynamics, J. Thorac. Cardiovasc. Surg. 137 (2) (2009) 394–403.
- [3] Rajat Mittal, Jung Hee Seo, Vijay Vedula, Young J Choi, Hang Liu, H Howie Huang, Saurabh Jain, Laurent Younes, Theodore Abraham, Richard T George, Computational modeling of cardiac hemodynamics: Current status and future outlook, J. Comput. Phys. 305 (2016) 1065–1082.
- [4] Vijay Vedula, Juhyun Lee, Hao Xu, C-C Jay Kuo, Tzung K Hsiai, Alison L Marsden, A method to quantify mechanobiologic forces during zebrafish cardiac development using 4-D light sheet imaging and computational modeling, PLoS Comput. Biol. 13 (10) (2017) e1005828.
- [5] Alberto Zingaro, Ivan Funagalli, Luca Dede, Marco Fedele, Pasquale Claudio Africa, Antonio Francesco Corno, Alfio Quarteroni, A geometric multiscale
- model for the numerical simulation of blood flow in the human left heart, 2021, arXiv preprint arXiv:2110.02114.

 [6] Mostafa Mahmoudi, Chadrick Jennings, Keith Pereira, Andrew F Hall, Amirhossein Arzani, Guiding the prostatic artery embolization procedure with computational fluid dynamics, J. Biomech. Eng. 144 (11) (2022) 111004.
- [7] Priya J Nair, Martin R Pfaller, Seraina A Dual, Michael Loecher, Doff B McElhinney, Daniel B Ennis, Alison L Marsden, Hemodynamics in patients with aortic coarctation: A comparison of in vivo 4D-flow MRI and FSI simulation, in: International Conference on Functional Imaging and Modeling of the Heart. Springer, 2023, pp. 515–523.
- [8] Brian Baillargeon, Nuno Rebelo, David D Fox, Robert L Taylor, Ellen Kuhl, The living heart project: a robust and integrative simulator for human heart function, Eur. J. Mech. A Solids 48 (2014) 38–47.
- [9] Marina Strocchi, Matthias AF Gsell, Christoph M Augustin, Orod Razeghi, Caroline H Roney, Anton J Prassl, Edward J Vigmond, Jonathan M Behar, Justin S Gould, Christopher A Rinaldi, et al., Simulating ventricular systolic motion in a four-chamber heart model with spatially varying robin boundary conditions to model the effect of the pericardium, J. Biomech. 101 (2020) 109645.
- [10] Elias Karabelas, Matthias AF Gsell, Gundolf Haase, Gernot Plank, Christoph M Augustin, An accurate, robust, and efficient finite element framework with applications to anisotropic, nearly and fully incompressible elasticity, Comput. Methods Appl. Mech. Engrg. 394 (2022) 114887.
- [11] Marco Fedele, Roberto Piersanti, Francesco Regazzoni, Matteo Salvador, Pasquale Claudio Africa, Michele Bucelli, Alberto Zingaro, Alfio Quarteroni, et al., A comprehensive and biophysically detailed computational model of the whole human heart electromechanics, Comput. Methods Appl. Mech. Engrg. 410 (2023) 115983.
- [12] Nicolás A. Barnafi, Luca F. Pavarino, Simone Scacchi, A comparative study of scalable multilevel preconditioners for cardiac mechanics, J. Comput. Phys. 492 (2023) 112421.
- [13] Matthew Hirschhorn, Vakhtang Tchantchaleishvili, Randy Stevens, Joseph Rossano, Amy Throckmorton, Fluid-structure interaction modeling in cardiovascular medicine—A systematic review 2017–2019, Med. Eng. Phys. 78 (2020) 1–13.
- [14] Michele Bucelli, Luca Dede, Alfio Quarteroni, Christian Vergara, et al., Partitioned and monolithic algorithms for the numerical solution of cardiac fluid-structure interaction, Commun. Comput. Phys. 32 (5) (2022) 1217–1256.
- [15] Michele Bucelli, Alberto Zingaro, Pasquale Claudio Africa, Ivan Fumagalli, Luca Dede', Alfio Quarteroni, A mathematical model that integrates cardiac electrophysiology, mechanics, and fluid dynamics: Application to the human left heart, Int. J. Numer. Methods Biomed. Eng. 39 (3) (2023) e3678.
- [16] Marshall Davey, Charles Puelz, Simone Rossi, Margaret Anne Smith, David R Wells, Greg Sturgeon, W Paul Segars, John P Vavalle, Charles S Peskin, Boyce E Griffith, Simulating cardiac fluid dynamics in the human heart, 2023, arXiv preprint arXiv:2307.02680.
- [17] Alfio Quarteroni, Alessandro Veneziani, Christian Vergara, Geometric multiscale modeling of the cardiovascular system, between theory and practice, Comput. Methods Appl. Mech. Engrg. 302 (2016) 193–252.
- [18] Irene E Vignon-Clementel, C Alberto Figueroa, Kenneth E Jansen, Charles A Taylor, Outflow boundary conditions for three-dimensional finite element modeling of blood flow and pressure in arteries, Comput. Methods Appl. Mech. Engrg. 195 (29–32) (2006) 3776–3796.
- [19] Mahdi Esmaily Moghadam, Irene E Vignon-Clementel, Richard Figliola, Alison L Marsden, Modeling of Congenital Hearts Alliance (MOCHA) Investigators, et al., A modular numerical method for implicit 0D/3D coupling in cardiovascular finite element simulations, J. Comput. Phys. 244 (2013) 63–79.
- [20] Marc Hirschvogel, Marina Bassilious, Lasse Jagschies, Stephen M Wildhirt, Michael W Gee, A monolithic 3d-0d coupled closed-loop model of the heart and the vascular system: experiment-based parameter estimation for patient-specific cardiac mechanics, Int. J. Numer. Methods Biomed. Eng. 33 (8) (2017) e2842.
- [21] Christoph M Augustin, Matthias AF Gsell, Elias Karabelas, Erik Willemen, Frits W Prinzen, Joost Lumens, Edward J Vigmond, Gernot Plank, A computationally efficient physiologically comprehensive 3D–0D closed-loop model of the heart and circulation, Comput. Methods Appl. Mech. Engrg. 386 (2021) 114092.

- [22] Francesco Regazzoni, Matteo Salvador, Pasquale Claudio Africa, Marco Fedele, Luca Dedè, Alfio Quarteroni, A cardiac electromechanical model coupled with a lumped-parameter model for closed-loop blood circulation, J. Comput. Phys. 457 (2022) 111083.
- [23] Lucia Carichino, Giovanna Guidoboni, Marcela Szopos, Energy-based operator splitting approach for the time discretization of coupled systems of partial and ordinary differential equations for fluid flows: The stokes case, J. Comput. Phys. 364 (2018) 235–256.
- [24] Sheikh Mohammad Shavik, Zhenxiang Jiang, Seungik Baek, Lik Chuan Lee, High spatial resolution multi-organ finite element modeling of ventricular-arterial coupling, Front. Physiol. 9 (2018) 119.
- [25] Roy CP Kerckhoffs, Maxwell L Neal, Quan Gu, James B Bassingthwaighte, Jeff H Omens, Andrew D McCulloch, Coupling of a 3D finite element model of cardiac ventricular mechanics to lumped systems models of the systemic and pulmonic circulation, Ann. Biomed. Eng. 35 (1) (2007) 1–18.
- [26] Arian Jafari, Edward Pszczolkowski, Adarsh Krishnamurthy, A framework for biomechanics simulations using four-chamber cardiac models, J. Biomech.
- [27] Will Zhang, Javiera Jilberto, Gerhard Sommer, Michael S Sacks, Gerhard A Holzapfel, David A Nordsletten, Simulating hyperelasticity and fractional viscoelasticity in the human heart, Comput. Methods Appl. Mech. Engrg. 411 (2023) 116048.
- [28] Ulrich Küttler, Christiane Förster, Wolfgang A. Wall, A solution for the incompressibility dilemma in partitioned fluid-structure interaction with pure Dirichlet fluid domains, Comput. Mech. 38 (2006) 417–429.
- [29] F. Regazzoni, Stabilization of staggered time discretization schemes for 0D-3D fluid-structure interaction problems, MOX Rep. 17 (2022).
- [30] Chi Zhu, Vijay Vedula, Dave Parker, Nathan Wilson, Shawn Shadden, Alison Marsden, svFSI: a multiphysics package for integrated cardiac modeling, J. Open Sour. Softw. 7 (78) (2022) 4118.
- [31] Kathrin Bäumler, Vijay Vedula, Anna M Sailer, Jongmin Seo, Peter Chiu, Gabriel Mistelbauer, Frandics P Chan, Michael P Fischbein, Alison L Marsden, Dominik Fleischmann, Fluid-structure interaction simulations of patient-specific aortic dissection, Biomech. Model. Mechanobiol. 19 (5) (2020) 1607–1628.
- [32] Ingrid S Lan, Weiguang Yang, Jeffrey A Feinstein, Jacqueline Kreutzer, R Thomas Collins, Michael Ma, Gregory T Adamson, Alison L Marsden, Virtual transcatheter interventions for peripheral pulmonary artery stenosis in williams and alagille syndromes, J. Am. Heart Assoc. 11 (6) (2022) e023532.
- [33] Noelia Grande Gutierrez, Mathew Mathew, Brian W McCrindle, Justin S Tran, Andrew M Kahn, Jane C Burns, Alison L Marsden, Hemodynamic variables in aneurysms are associated with thrombotic risk in children with kawasaki disease, Int. J. Cardiol. 281 (2019) 15–21.
- [34] Tony F. Chan, An approximate Newton method for coupled nonlinear systems, SIAM J. Numer. Anal. 22 (5) (1985) 904-913.
- [35] Mahdi Esmaily-Moghadam, Yuri Bazilevs, Alison L. Marsden, A new preconditioning technique for implicitly coupled multidomain simulations with applications to hemodynamics, Comput. Mech. 52 (5) (2013) 1141–1152.
- [36] Ethan Kung, Alessia Baretta, Catriona Baker, Gregory Arbia, Giovanni Biglino, Chiara Corsini, Silvia Schievano, Irene E Vignon-Clementel, Gabriele Dubini, Giancarlo Pennati, et al., Predictive modeling of the virtual hemi-fontan operation for second stage single ventricle palliation: two patient-specific cases, J. Biomech. 46 (2) (2013) 423–429.
- [37] Joaquim Peiró, Alessandro Veneziani, Reduced models of the cardiovascular system, in: Cardiovascular Mathematics: Modeling and Simulation of the Circulatory System, Springer, 2009, pp. 347–394.
- [38] Stefan Artlich, Wolfgang Mackens, Newton-coupling of fixed point iterations, in: Numerical Treatment of Coupled Systems, Springer, 1995, pp. 1-10.
- [39] Hermann G. Matthies, Jan Steindorf, Partitioned strong coupling algorithms for fluid-structure interaction, Comput. Struct. 81 (8-11) (2003) 805-812.
- [40] Joris Degroote, Partitioned simulation of fluid-structure interaction: Coupling black-box solvers with quasi-Newton techniques, Arch. Comput. Methods Eng. 20 (3) (2013) 185–238.
- [41] Michele Benzi, Gene H. Golub, Jörg Liesen, Numerical solution of saddle point problems, Acta Numer. 14 (2005) 1-137.
- [42] D.J. Evans, The analysis and application of sparse matrix algorithms in the finite element method, in: The Mathematics of Finite Elements and Applications, Elsevier, 1973, pp. 427–447.
- [43] Jongmin Seo, Daniele E. Schiavazzi, Alison L. Marsden, Performance of preconditioned iterative linear solvers for cardiovascular simulations in rigid and deformable vessels, Comput. Mech. 64 (3) (2019) 717–739.
- [44] David Eberly, Triangulation by ear clipping, Geom. Tools (2008) 2002–2005.
- [45] W. Schroeder, K. Martin, B. Lorensen, The Visualization Toolkit, 4th ed., Kitware, New York, 2006.
- [46] Sander Land, Viatcheslav Gurev, Sander Arens, Christoph M Augustin, Lukas Baron, Robert Blake, Chris Bradley, Sebastian Castro, Andrew Crozier, Marco Favino, et al., Verification of cardiac mechanics software: benchmark problems and solutions for testing active and passive material behaviour, Proc. R. Soc. A: Math. Phys. Eng. Sci. 471 (2184) (2015) 20150641.
- [47] Dominique Chapelle, Patrick Le Tallec, Philippe Moireau, Michel Sorine, Energy-preserving muscle tissue model: formulation and compatible discretizations, Int. J. Multiscale Comput. Eng. 10 (2) (2012).
- [48] Martin R Pfaller, Julia M Hörmann, Martina Weigl, Andreas Nagler, Radomir Chabiniok, Cristóbal Bertoglio, Wolfgang A Wall, The importance of the pericardium for cardiac biomechanics: from physiology to computational modeling, Biomech. Model. Mechanobiol. 18 (2019) 503–529.
- [49] Gerhard A. Holzapfel, Ray W. Ogden, Constitutive modelling of passive myocardium: a structurally based framework for material characterization, Phil. Trans. R. Soc. A 367 (1902) (2009) 3445–3475.
- [50] Ateet Kosaraju, Amandeep Goyal, Yulia Grigorova, Amgad N Makaryus, Left ventricular ejection fraction, 2017.
- [51] Afshin Anssari-Benam, Andrea Bucchi, Giuseppe Saccomandi, Modelling the inflation and elastic instabilities of rubber-like spherical and cylindrical shells using a new generalised neo-hookean strain energy function, J. Elasticity 151 (1) (2022) 15–45.
- [52] Millard F. Beatty, Topics in finite elasticity: hyperelasticity of rubber, elastomers, and biological tissues—with examples, 1987.
- [53] L.A. Taber, B.B. Keller, E.B. Clark, Cardiac mechanics in the stage-16 chick embryo, 1992.
- [54] Nabid Salehin, Cameron Villarreal, Tanveer Teranikar, Benjamin Dubansky, Juhyun Lee, Cheng-Jen Chuong, Assessing pressure-volume relationship in developing heart of zebrafish in-vivo, Ann. Biomed. Eng. (2021) 1–14.
- [55] MA1913032 Crisfield, An arc-length method including line searches and accelerations, Internat. J. Numer. Methods Engrg. 19 (9) (1983) 1269-1289.
- [56] Daniele E Schiavazzi, Ethan O Kung, Alison L Marsden, Catriona Baker, Giancarlo Pennati, Tain-Yen Hsia, Anthony Hlavacek, Adam L Dorfman, Modeling of Congenital Hearts Alliance (MOCHA) Investigators, et al., Hemodynamic effects of left pulmonary artery stenosis after superior cavopulmonary connection: a patient-specific multiscale modeling study, J. Thorac. Cardiovasc. Surg. 149 (3) (2015) 689–696.
- [57] Weiguang Yang, Melody Dong, Marlene Rabinovitch, Frandics P Chan, Alison L Marsden, Jeffrey A Feinstein, Evolution of hemodynamic forces in the pulmonary tree with progressively worsening pulmonary arterial hypertension in pediatric patients, Biomech. Model. Mechanobiol. 18 (2019) 779–796.
- [58] Erica L Schwarz, John M Kelly, Kevin M Blum, Kan N Hor, Andrew R Yates, Jacob C Zbinden, Aekaansh Verma, Stephanie E Lindsey, Abhay B Ramachandra, Jason M Szafron, et al., Hemodynamic performance of tissue-engineered vascular grafts in fontan patients, NPJ Regen. Med. 6 (1) (2021) 38.
- [59] Ju Liu, Alison L. Marsden, A unified continuum and variational multiscale formulation for fluids, solids, and fluid-structure interaction, Comput. Methods Appl. Mech. Engrg. 337 (2018) 549–597.
- [60] David Nordsletten, Adela Capilnasiu, Will Zhang, Anna Wittgenstein, Myrianthi Hadjicharalambous, Gerhard Sommer, Ralph Sinkus, Gerhard A Holzapfel, A viscoelastic model for human myocardium, Acta Biomater. 135 (2021) 441–457.
- [61] P.J. Blanco, R.A. Feijóo, S.A. Urquiza, A unified variational approach for coupling 3D-1D models and its blood flow applications, Comput. Methods Appl. Mech. Engrg. 196 (41-44) (2007) 4391-4410.
- [62] Etienne Boileau, Perumal Nithiarasu, Pablo J Blanco, Lucas O Müller, Fredrik Eikeland Fossan, Leif Rune Hellevik, Wouter P Donders, Wouter Huberts, Marie Willemet, Jordi Alastruey, A benchmark study of numerical schemes for one-dimensional arterial blood flow modelling, Int. J. Numer. Methods Biomed. Eng. 31 (10) (2015) e02732.

- [63] Matteo Salvador, Marco Fedele, Pasquale Claudio Africa, Eric Sung, Adityo Prakosa, Jonathan Chrispin, Natalia Trayanova, Alfio Quarteroni, et al., Electromechanical modeling of human ventricles with ischemic cardiomyopathy: numerical simulations in sinus rhythm and under arrhythmia, Comput. Biol. Med. 136 (2021) 104674.
- [64] Matteo Salvador, Francesco Regazzoni, Stefano Pagani, Natalia Trayanova, Alfio Quarteroni, et al., The role of mechano-electric feedbacks and hemodynamic coupling in scar-related ventricular tachycardia, Comput. Biol. Med. 142 (2022) 105203.
- [65] Piero Colli Franzone, Luca Franco Pavarino, Simone Scacchi, Mathematical Cardiac Electrophysiology, Vol. 13, Springer, 2014.
- [66] Miguel Guerra, Francisco Sampaio, Carmen Bras-Silva, Adelino F Leite-Moreira, Left intraventricular diastolic and systolic pressure gradients, Exp. Biol. Med. 236 (12) (2011) 1364–1372.
- [67] Hiroyuki Iwano, Daisuke Kamimura, Ervin Fox, Michael Hall, Pavlos Vlachos, William C Little, Altered spatial distribution of the diastolic left ventricular pressure difference in heart failure, J. Am. Soc. Echocardiogr. 28 (5) (2015) 597–605.
- [68] Katsuhiro Matsuura, Kenjirou Shiraishi, Kotomi Sato, Kazumi Shimada, Seijirow Goya, Akiko Uemura, Mayumi Ifuku, Takeshi Iso, Ken Takahashi, Ryou Tanaka, Left ventricular vortex and intraventricular pressure difference in dogs under various loading conditions, Am. J. Physiol.-Heart Circ. Physiol. 316 (4) (2019) H882–H888.
- [69] Andrew Yeckel, Lisa Lun, Jeffrey J. Derby, An approximate block Newton method for coupled iterations of nonlinear solvers: Theory and conjugate heat transfer applications, J. Comput. Phys. 228 (23) (2009) 8566–8588.